Monthly Notices of the ROYAL ASTRONOMICAL SOCIETY

MNRAS **527,** 11521–11538 (2024) https://doi.org/10.1093/mnras/stad3761
Advance Access publication 2023 September 12

Modelling the seasonal cycle of Uranus's colour and magnitude, and comparison with Neptune

Patrick G. J. Irwin [1]★ Jack Dobinson,[1] Arjuna James [1] Nicholas A. Teanby [2] Amy A. Simon [3] Leigh N. Fletcher [4] Michael T. Roman [4] Glenn. S. Orton [5] Michael H. Wong [6] Daniel Toledo [7] Santiago Pérez-Hoyos [8] and Julie Beck [9]

[1]*Atmospheric, Oceanic and Planetary Physics, Department of Physics, University of Oxford, Parks Road, Oxford OX1 3PU, UK*
[2]*School of Earth Sciences, University of Bristol, Wills Memorial Building, Queens Road, Bristol BS8 1RJ, UK*
[3]*Solar System Exploration Division/690, NASA Goddard Space Flight Center, 8800 Greenbelt Rd, Greenbelt, MA 20771, USA*
[4]*School of Physics & Astronomy, University of Leicester, University Road, Leicester, LE1 7RH, UK*
[5]*Jet Propulsion Laboratory, California Institute of Technology, 4800 Oak Grove Drive, Pasadena, CA 91109, USA*
[6]*Center for Integrative Planetary Science, University of California, Berkeley, CA 94720-3411, USA*
[7]*Instituto Nacional de Técnica Aeroespacial (INTA), E-28850, Torrejón de Ardoz, Madrid, Spain*
[8]*University of the Basque Country UPV/EHU, E-48013 Bilbao, Spain*
[9]*Department of Physics, Institute for Particle Physics and Astrophysics, ETH Zurich, CH-8093 Zurich, Switzerland*

Accepted 2023 December 2. Received 2023 November 29; in original form 2023 October 13

ABSTRACT

We present a quantitative analysis of the seasonal record of Uranus's disc-averaged colour and photometric magnitude in Strömgren *b* and *y* filters (centred at 467 and 551 nm, respectively), recorded at the Lowell Observatory from 1950 to 2016, and supplemented with *HST*/WFC3 observations from 2016 to 2022. We find that the seasonal variations of magnitude can be explained by the lower abundance of methane at polar latitudes combined with a time-dependent increase of the reflectivity of the aerosol particles in layer near the methane condensation level at 1 – 2 bar. This increase in reflectivity is consistent with the addition of conservatively scattering particles to this layer, for which the modelled background haze particles are strongly absorbing at both blue and red wavelengths. We suggest that this additional component may come from a higher proportion of methane ice particles. We suggest that the increase in reflectivity of Uranus in both filters between the equinoxes in 1966 and 2007, noted by previous authors, might be related to Uranus's distance from the Sun and the production rate of dark photochemical haze products. Finally, we find that although the visible colour of Uranus is less blue than Neptune, due to the increased aerosol thickness on Uranus, and this difference is greatest at Uranus's solstices, it is much less significant than is commonly believed due to a long-standing misperception of Neptune's 'true' colour. We describe how filter-imaging observations, such as those from Voyager-2/ISS and *HST*/WFC3, should be processed to yield accurate true colour representations.

Key words: planets and satellites: atmospheres – radiative transfer – scattering – techniques: photometric.

1 INTRODUCTION

Uranus and Neptune, the so-called 'Ice Giants', are the most distant giant planets in our Solar system and the most difficult to study, given their low magnitude and small apparent disc sizes of only ∼3.8" and ∼2.4", respectively. They both appear blue-green to naked-eye astronomers as their atmospheres contain a significant mole fraction of methane gas (2 – 5 per cent) (Atreya et al. 2020) in their observable atmospheres, which has prominent absorption bands at green and red wavelengths, shown in Fig. 1 as spectral plots, and also as an astronomer would view these planets through a spectroscope. These absorption bands were first detected in the 19th Century, while the suggestion that these bands were due to methane absorption was made in the early 1930s (Wildt 1934a, b) and confirmed by spectroscopic observations at Lowell Observatory (Adel & Slipher 1934).

Our knowledge of these worlds was revolutionized by the flybys of the NASA Voyager 2 spacecraft on 1986 January 24 and 1989 August 25, respectively, which made the first high spatial resolution observations. Since these Voyager encounters, our perception of the visible appearance of these worlds comes primarily from images reconstructed from observations from Voyager 2's Imaging Science System (ISS), which recorded images in several separate filters, running from UV to orange (290 – 650 nm). These images were then combined to give composite visual images such as those shown in Fig. 2. In these Voyager-2/ISS images, Uranus[1] (Fig. 2a) appears pale green, while Neptune[2] (Fig. 2b) appears darker blue, and this perception of the relative colours of these planets has become commonly accepted. However, although the early Uranus images were processed

[1]https://tinyurl.com/426jz9bp
[2]https://www.nasa.gov/feature/jpl/30-years-ago-voyager-2s-historic-neptune-flyby

★ E-mail: patrick.irwin@physics.ox.ac.uk

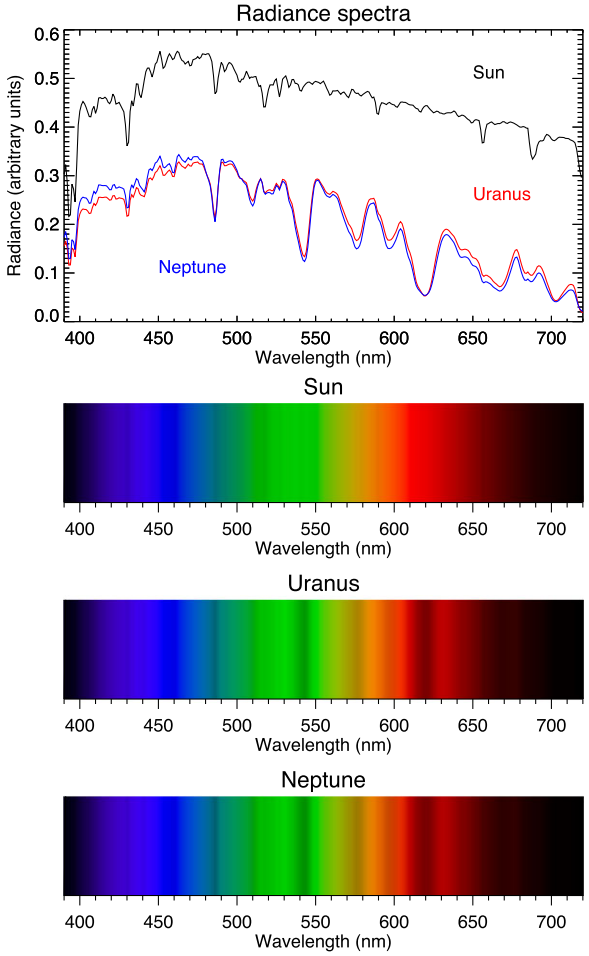

Figure 1. Top panel: Disc-averaged radiance spectra of Uranus and Neptune, compared to the spectrum of a perfectly reflecting Lambertian surface at the same solar distance (i.e. 'Sun'). Bottom panels compare the same three spectra (normalized) as viewed through a long-slit spectrometer to demonstrate the efficacy of the colour-rendering procedure described in this paper. The solar spectrum is that of Chance & Kurucz (2010) and the calculations also include the transmission spectrum of a standard Earth atmosphere to simulate ground-based observations. The Uranus and Neptune spectra are constructed from disc-averages of *Hubble Space Telescope (HST)*/Space Telescope Imaging Spectrograph (STIS) reflectivity observations from 2002 (Karkoschka & Tomasko 2009) and 2003 (Karkoschka & Tomasko 2011), respectively, multiplied by the solar and terrestrial atmosphere spectra. Fraunhofer absorption lines from the Solar atmosphere are faintly seen in all three spectra, but prominent dark absorption bands at green and red wavelengths are also seen the the spectra of Uranus and Neptune, which is caused by atmospheric methane absorption. It is this absorption that gives these planets their distinctive blue-green colour.

to yield approximately their 'true' colour, the early-Neptune images were contrast-enhanced to accentuate fainter features and do not accurately represent the true colour of this planet. This was well known and of concern to planetary scientists at the time, and followed on from earlier debates on how the Voyager images of Jupiter and Saturn should best be presented (e.g. Young 1985). However, the subtleties of how these filter-imaging observations were combined to generate colour images was lost on the general public. In more recent reconstructions, showing the 'true' colour of these planets[3],

[3]https://www.planetary.org/articles/uranus-neptune-color-difference

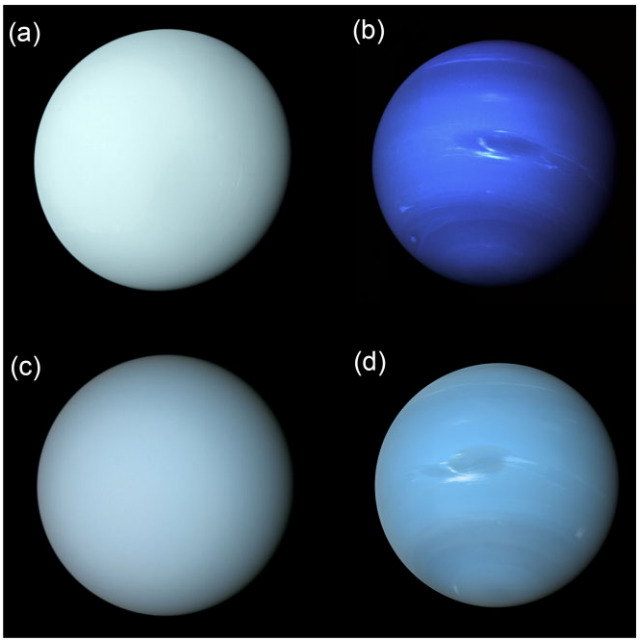

Figure 2. Panels a and b show early images of the visible appearance of Uranus and Neptune reconstructed from Voyager 2 ISS images in 1986 and 1989, respectively, showing Uranus to be pale blue-green, and Neptune dark blue (PIA18182 and PIA01492, credit: NASA/JPL-Caltech). While these early Uranus images were close to 'true' colour, the Neptune images were actually stretched and enhanced. Panels c and d show more recent reconstructions of the true colours of these planets, showing them to be more similarly coloured (credit: NASA/JPL-Caltech/Björn Jónsson, https://www.planetary.org/articles/uranus-neptune-color-difference).

they can be seen to be more similarly coloured (Fig. 2c and d), consistent with the similarity of their reflectance spectra shown in Fig. 1.

Since the Voyager 2 encounters, Uranus and Neptune have remained the subject of detailed study from both ground-based telescopes, whose spatial and spectral performance has improved immensely over the intervening 30–40 yr, and also with the *Hubble Space Telescope (HST)*. As Uranus moved past its southern summer solstice in 1986, it was noted that the polar region appeared to be brighter than equatorial latitudes, as though covered with a 'hood' of brighter material, which appeared to fade as Uranus approached northern summer equinox in 2007. Rages, Hammel & Friedson (2004) interpreted the diminishing brightness of the polar region after the Voyager encounter as a decline in the optical depth of the methane cloud, placed between 1.26 and 2 bars. Approaching the 2007 equinox, the hood receded to a bright residual zone at 45°S, which Sromovsky & Fry (2008) found was likely associated with increased aerosol scattering in a cloud layer near the 2-bar bar level. Sromovsky et al. (2009) compared the north and south polar zones from 2004 to 2007 from Keck-II/NIRC2 (H-band) and *HST*/Wide Field Camera 2 (WFC2; 924-nm) images and determined centre-to-limb reflectance variations showing yearly trends that mirror those determined from later *HST*/WFC3 observations (2015–2021) by James et al. (2023), and which are found to be consistent with changes in the reflectivity of aerosols near 1–2 bar. Toledo et al. (2018) note that the reduced abundance of methane near Uranus's poles contributes greatly to the relative brightness of the polar region observed in H-band observations by Very Large Telescope (VLT)/SINFONI in 2014 and is likely a contributing factor at visible

wavelengths also. However, Sromovsky et al. (2019) and James et al. (2023) find this effect is secondary to the variations in the aerosol reflectivity near 1–2 bar.

In a recent comparative study, Irwin et al. (2022) modelled observations of both Uranus and Neptune from 2002 to 2010, made with (1) *HST*'s Space Telescope Imaging Spectrograph (STIS); (2) the SpeX instrument of the NASA's Infrared Telescope Facility (IRTF); and (3) Gemini-North's Near-Infrared Integral Field Spectrometer (NIFS). These data, covering a wide range of wavelengths from 0.3 to 2.4 μm, enabled Irwin et al. (2022) to develop an 'holistic', simple model for the haze and cloud structure of both planetary atmospheres, consisting of (1) a deep layer of aerosol (Aerosol-1) extending up to the ∼5 bar level (the limiting pressure of sensitivity), composed most likely of photochemical haze and H_2S ice; (2) a middle layer of aerosol at ∼2 bar (Aerosol-2), composed most likely of photochemical haze and methane ice; and (3) and extended layer of photochemical haze (Aerosol-3) reaching up from the Aerosol-2 level into the lower stratosphere. An unexpected by-product of this new 'holistic' model was that it can explain why Neptune is bluer than Uranus since the opacity of Neptune's Aerosol-2 layer at ∼2 bar is found to be roughly half that of Uranus. This allows light to penetrate deeper into Neptune's atmosphere before being reflected, leading to more absorption by red-absorbing gaseous methane and so making the planet appear bluer. When Irwin et al. (2022) compared the predicted visual colours from the *HST*/STIS observations of Uranus and Neptune, it was apparent that although Uranus was slightly more green than Neptune, the difference in colour was understandably nothing like as extreme as that shown in the early Voyager 2 observations (Figs 2a and b), where the Neptune images were contrast-enhanced as previously outlined. The reconstructed colours were more similar to later 'true' colour renderings (Figs 2c and d), but not identical, and we wondered if it might be possible to determine quantitatively whether there has been any significant change in the colours of Uranus and Neptune since the late-1980s.

Fortunately, there exists an historical data set that can be used to address some of these questions. The disc-integrated magnitudes of Uranus and Neptune have been monitored since 1950 by observers at the Lowell Observatory (Lockwood & Jerzykiewicz 2006; Lockwood 2019), with Johnson B and V magnitudes (of the UBV photometric system), centred at 445 and 551 nm, respectively, monitored from 1950 to 1966, and Strömgren *b* and *y* magnitudes (blue and green, centred at 467 and 551 nm, respectively) recorded from 1972 to 2016. The filter profiles of these observations are compared later in Fig. 9. For Uranus, these unique Lowell data show seasonal changes in the magnitude in these blue and green filters, with maximum brightness seen at Uranus's solstices, and minimum brightness seen at the equinoxes, but with magnitude in the Strömgren *y* and Johnson V filters changing much more significantly than Strömgren *b* and Johnson B. This indicates a clear seasonal change in Uranus's colour, with Uranus appearing less blue at the solstices (for reference, the Voyager 2 flyby of Uranus was shortly after the 1985 summer southern solstice). Hammel & Lockwood (2007) also noted that Uranus was darker near the equinox in 1966 than it was near the equinox in 2007, suggesting annual variability on top of these biannual solstice variations. In addition, as a secondary effect, small variations in magnitude were noted by Aplin & Harrison (2017), which are approximately correlated with the solar cycle.

For Neptune, the Lowell data record a steady increase in disc-integrated brightness over the period of observation in both channels, but no significant change in colour. This increase in brightness appears to be inversely correlated with Neptune's solar distance (Hammel & Lockwood 2007), although it is unclear if there is a causal connection. However, these long-term albedo changes of Neptune are complicated by its dynamic cloud activity. Lockwood & Thompson (2002) found there to be a non-seasonal component in Neptune's magnitude, which was found to be correlated with the 11-yr solar cycle. Furthermore, they noted similar variations in the brightness at near-infrared wavelengths, but with an amplitude 20–50 times larger and concluded that the variation in the Sun's UV flux at Neptune was modulating the upper tropospheric cloud cover. Aplin & Harrison (2016) reanalysed these data (together with more recent magnitude determinations) and concluded that modulation of Galactic Cosmic Rays (GCRs) by the solar cycle might be a more important link with cloud cover. Roman et al. (2022) also find a correlation between the solar cycle and the mid-infrared brightness of Neptune, suggesting higher stratospheric temperatures and abundances of photochemical products (e.g., ethane) at solar maxima. Most recently, Chavez et al. (2023) has found a strong correlation between the occurrence of upper-tropospheric (0.1–0.6 bar) methane ice clouds and the solar activity and suggest that increased abundances of photochemical products, such as ethane, seed cloud formation, which will increase the overall planetary albedo.

In addition to these Lowell disc-integrated brightness measurements, we also have very good observations of how Uranus's spatially resolved visible reflectance spectrum has evolved since the early-2000s, which we can use to supplement and enhance these data. These data come the STIS and WFC2 and WFC3 instruments on *HST*, and more recently the MUSE instrument at the European Southern Observatory's (ESO) VLT in Chile. In this paper we aim to understand the true visible colour cycle of Uranus, and construct a model of Uranus's atmosphere that matches and explains the seasonal cycle of Uranus's blue and green reflectances recorded in the disc-integrated Lowell Observatory photometry data and also matches the imaging observations. The observations that we analyse and compare come from several different sources, and we will show that the rendering of these data to 'true' colour is a surprisingly nuanced and subtle procedure. In Section 2, we review the existing sources of Uranus imaging observations and demonstrate how they can be most accurately processed to determine visible colour. In Section 3, we then use these imaging data to supplement the photometric magnitude data set and help interpret them. We discuss our analysis in Section 4 and present our conclusions in Section 5.

2 DISC-RESOLVED OBSERVATIONS OF URANUS

In this section, we will review the different sources of disc-resolved imaging data of Uranus used in this study to complement and interpret the Lowell photometric data of Lockwood & Jerzykiewicz (2006) and Lockwood (2019). We will describe how these observations should be processed to produce 'true' colour images representing the appearance of these planets to the average human eye. These observations comprise both spectroscopic-imaging and filter-imaging observations.

2.1 Spectroscopic-imaging observations

Spectroscopic imaging encompasses observations where images are recorded at thousands of wavelengths near-simultaneously. This can be achieved either by stepping the entrance slit of a long-slit spectrometer sequentially across an object, in a direction orthogonal to the slit, or by the use of Integral Field Unit (IFU) spectrometers, which optically split the light entering different parts of the instrument field of view onto different parts of a grating to simultaneously

record a spectral image. The resulting product of spectroscopic-imaging observations is a spectral imaging 'cube', where each pixel (or 'spaxel') of the image contains a complete spectrum. The two sets of data analysed in this study come from *HST*/STIS and VLT/MUSE.

2.1.1 HST/*STIS*

Three sets of Uranus observations from the STIS on the *HST* are considered in this study, recorded in September 2002 (Karkoschka & Tomasko 2009), September 2012 (Sromovsky et al. 2014), and October 2015 (Sromovsky et al. 2019). The observations were made with the long-slit parallel to Uranus's central meridian and spectra along the slit recorded for multiple horizontal offsets of the slit, starting on the central meridian and then sequentially stepping towards the evening, left-hand limb,[4] with Uranus's north pole at the top. Hence, the combined data set from one of these observations forms a cube of half the planet. The data from 2002 were analysed by Irwin et al. (2022) to help determine their 'holistic' model of the vertical aerosol structure in the atmospheres of Uranus and Neptune. These data and the subsequent data sets from 2012 and 2015 were further analysed by James et al. (2023), as discussed later.

The reflectance spectra of Uranus recorded by *HST*/STIS cover the spectral range 300–1000 nm, with a step of 1 nm and spectral resolution of 2 nm. To construct the appearance of Uranus to the naked eye from these observations, we first need for each pixel to transform the measured reflectance spectrum to a radiance spectrum (i.e., $\mathrm{W\,m^{-2}\,sr^{-1}\,\mu m^{-1}}$), which was done by multiplying the recorded reflectances by the radiance spectrum of sunlight reflected from a perfectly reflecting Lambertian surface at Uranus's distance from the Sun. The solar spectrum used in this calculation was that of Chance & Kurucz (2010). Then, the radiance spectrum needs to be converted to 'tri-stimulus' values to simulate their apparent colours to the 'average' human eye (see Appendix A), multiplying by the colour-matching functions of the XYZ colour space of the Commission Internationale de l'Éclairage (CIE) and integrating, and then transforming the resulting XYZ colours to the standard RGB (sRGB) colour space (e.g. Stockman & Sharpe 2000; Stockman 2019). This process reduces the spectrum at each pixel to its three-colour sRGB representation. Finally, computer monitors and printers all assume that images to be displayed have had their intensities, I, Gamma-corrected (see Appendix A for more details) with a function such as

$$I_{\mathrm{corrected}} = \begin{cases} 12.92I, & I \leq 0.0031308 \\ 1.055I^{1/\gamma} - 0.055, & I > 0.0031308 \end{cases}, \quad (1)$$

where $\gamma = 2.4$. The Gamma correction makes the digitization of images more efficient, but must be corrected for when displaying the image, which is automatically done by all monitors and printers. Therefore, the computed intensities in our calculated images were themselves Gamma-corrected to ensure that they would appear on a monitor, or when printed, with the correct variation of intensity across the disc as perceived by an average human observing these planets through a telescope.

The resulting 'true' colour appearances of Uranus recorded by *HST*/STIS in 2002, 2012, and 2015 are shown in Fig. 3. Here it can be seen that at equatorial latitudes the colour of Uranus is slightly bluer than might be expected from the Voyager 2 images, but the 2002 image has a paler greenish colour south of 35°S. The observation in 2002 was made five years before Uranus's northern summer equinox in 2007, when the paler south polar region was clearly visible. By 2012, the south polar region had mostly swung out of view, and the north polar region was visible with a similar geometry to the south seen in 2002. However, the north polar region at this time was only slightly paler than mid-latitudes. By 2015, the paleness of the north polar region can be seen to have increased slightly from 2012 and the colour of the north polar region was approaching the colour of the south polar region viewed in 2002, although still rather less pale.

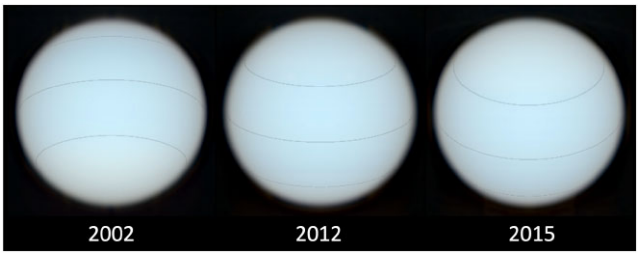

Figure 3. True colour appearance of Uranus reconstructed by the authors from *HST*/STIS observations in 2002, 2012, and 2015, respectively. Latitude lines at the equator and 35° N and S are marked. The images have been Gamma-corrected and the right-hand side of the images are simply reflections of the left-hand sides to make these images appear as discs, rather than half-discs. In all cases the north pole is at the top of the images. The very slightly paler polar regions are seen at the bottom of the 2002 image and at the top of the 2012 and 2015 images.

2.1.2 *VLT/MUSE*

Observations of Uranus were made with the MUSE instrument at the Very Large Telescope (VLT) in November 2021. MUSE is an IFU spectrometer, where each pixel (or 'spaxel') in its 300 × 300 pixel image is a spectrum covering 473–933 nm at a spectral resolution of ~3000. While VLT/MUSE has excellent spatial resolution, achieved with adaptive optics, the performance at short wavelengths is not sufficient to perceive subtle intensity variations. Hence, as part of a study to analyse VLT/MUSE observations of Neptune (Irwin et al. 2023a), a spatial deconvolution method was developed, MODIFIED-CLEAN, which has also been applied to these Uranus observations to improve their sharpness. For easy comparison with the *HST*/STIS data and compatibility with the methane absorption coefficients of Karkoschka & Tomasko (2010) used to model these observations, the MUSE spectra were smoothed to the same resolution of 2 nm and sampled every 1 nm. Converting these observations to apparent colour is complicated by two things (1) MUSE does not cover blue visible wavelengths from 400 to 473 nm and (2) the wavelengths 585–602 nm are not available as they are reserved for the laser guide star system necessary for the instrument's adaptive optics. Hence, for each pixel the missing wavelengths (400–473 nm, and 585–602 nm) were reconstructed from the disc-average analysis of the 2002 *HST*/STIS observations of Irwin et al. (2022), who fitted the data with a Minnaert limb-darkening model (equation (2)), where at each wavelength the reflectance (I/F) is approximated by

$$(I/F) = (I/F)_0 \mu_0^k \mu^{k-1}. \quad (2)$$

Here, μ and μ_0 are the cosines of the viewing and solar zenith angles, and $(I/F)_0$ and k are the fitted nadir reflectances and limb-darkening coefficients, respectively. At each point on the disc, a spectrum was reconstructed from these Minnaert coefficients at the local observed zenith angles, scaled to match the MUSE spectrum at

[4]Uranus's rotation is by convention retrograde, with its north pole accepted to be that which points above of the 'Invariable Plane'.

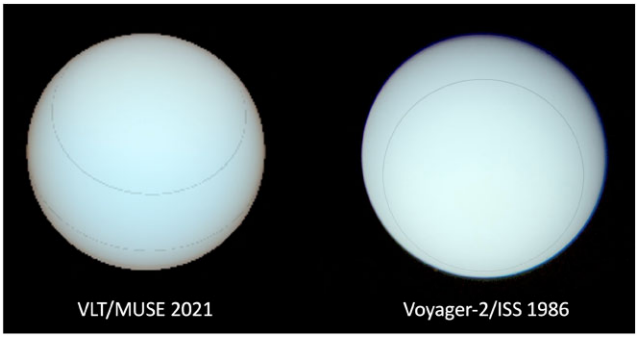

Figure 4. Visible appearance of Uranus reconstructed by the authors from deconvolved VLT/Multi-Unit Spectroscopic Explorer (MUSE) observations in 2021 (Left) and from Voyager-2/ISS filter images (violet:2661117, blue:2661022, green:2660720, orange:2660742) in 1986 (Right). For the MUSE image, the data have first been reconstructed from Minnaert fits to the limb-darkening at each latitude and wavelength to smooth over instrumental artefacts before conversion to true colour. For reference, latitude lines at the equator and 35° N and S are marked. These images have been rotated to align the south pole towards the bottom in both cases, for easy comparison.

the wavelengths of overlap, and then used as a substitute spectrum for the missing wavelengths. This was done separately for the 400–473 nm, and 585–602 nm windows. Then, the same procedure was followed as was used to convert the *HST*/STIS observations to true colour, converting the full reconstructed 400–800 nm spectra at each pixel to the XYZ and then to the sRGB colour spaces. The resulting Gamma-corrected VLT/MUSE image of Uranus (processed to remove instrumental artefacts) is shown in Fig. 4. In this image, observed six years after the *HST*/STIS observation of 2015, we can see the north pole pointing even more directly towards the Sun and the Earth, with the northern polar regions clearly significantly less blue than mid-latitudes.

2.2 Filter-imaging observations

In filter-imaging observations, the planet is observed with a discrete set of spectral filters allowing imaging at multiple target wavelengths, which can then be used to reconstruct colour images. Two sets of data are considered in this study from the *HST* WFC3 and the Voyager 2 ISS. The position and shape of the spectral filters of these instruments relative to an average Uranus spectrum and the cone responsivities of the average human eye are shown in Fig. 5. Here the Voyager/ISS filter responses are those of Danielson et al. (1981), while the *HST*/WFC3 filter profiles come from the instrument support documentation[5]

2.2.1 HST/WFC3

Observations of Uranus with the *HST*/WFC3 have been made annually since 2014 under the Outer Planetary Atmospheres Legacy (OPAL) programme (Simon, Wong & Orton 2015). These observations have been made using the filter set: F467M, F547M, FQ619N, F657N (2015 onwards), F658N (2014 only), FQ727N, F763M (2015 onwards), F845M, and FQ924N (2014 only). To accurately construct true colour images from these filter-imaging data requires that we have a reference model for what we believe the mean reflectance spectrum of Uranus to be. We can then use the measured reflectivities in the various filter channels to adjust the expected spectrum across the planet to be consistent with the observations and then transform the resulting adjusted spectrum to true colour in exactly the way as previously described for *HST*/STIS and VLT/MUSE. For the reference spectrum we used an equatorial average of the 2002 *HST*/STIS observations, averaging over all latitudes between 35°S and 35°N, which is shown in Fig. 5, together with the l_{10}, m_{10} and s_{10} cone responsivities of the average human eye (see Appendix A), which we label here as R_{eye}, G_{eye}, and B_{eye}, respectively. We chose an equatorial average rather than a disc average as the reflectivity of the equatorial regions is thought to be largely invariant with time, in contrast to the polar regions. Then, averaging these spectra over the WFC3 filter profiles (also shown in Fig. 5), we calculated the expected filter reflectivities in each pixel that were compared with those observed to calculate a correction factor $y_i = R_i(\text{meas})/R_i(\text{model})$ at each central filter wavelength λ_i, with i in the range 1 to N, and N is the number of filter channels used. A correction spectrum $y(\lambda)$ was then made by linearly interpolating between the (λ_i, y_i) values, with $y(\lambda)$ set to y_1 for $\lambda < \lambda_1$ and set to y_N for $\lambda > \lambda_N$. The reference Uranus spectrum was multiplied by this correction spectrum at each point and the resulting spectrum converted to XYZ and sRGB as before. Many of the WFC3 filters used are beyond the sensitivity of the human eye, while others are very narrow and sense upper tropospheric haze (e.g. FQ619N, FQ727N). Hence for this conversion, the filters used to adjust the reference spectrum were: F467M, F547M, and either F658N (2014) or F657N (2015 onwards). The resulting true colour Gamma-corrected appearances of Uranus observed by *HST*/WFC3 from 2014 to 2022 are shown in Fig. 6. Here, as the years progress, we can see the north pole rotating towards us and the north polar region becoming paler with time.

2.2.2 Voyager-2/ISS

Voyager 2's Imaging Science Subsystem (ISS) recorded numerous filter-averaged images of Uranus during its approach and flyby of Uranus in January 1986 (Smith et al. 1986). The NAC of ISS viewed in 'Clear', 'UV', 'Violet', 'Blue', 'Green', and 'Orange' filters, shown in Fig. 5, while its Wide Angle Camera (WAC) observed in very similar filters, but also included two other narrower filters, centred on methane absorption features. Although the camera lacked red filters, a set of NAC observations made during the approach of Uranus (2661117: violet, 2661022: blue, 2660720: green, 2660742: orange), were converted to true colour following exactly the same procedure as just outlined for the *HST*/WFC3 observations, except that as the Voyager/ISS images are recorded in units of reflectivity, they first had to be multiplied by the relevant channel-averaged solar spectrum to convert them to radiance. For this we again used the solar spectrum of Chance & Kurucz (2010). The resulting Gamma-corrected image is compared with that derived from our VLT/MUSE 2021 observations in Fig. 4. As can be seen, there is good agreement between the apparent colour of Uranus observed by Voyager 2 in 1986 compared with more recent determinations, although it appears slightly less blue, due almost certainly to the polar 'hood' covering a larger part of Uranus's disc. Note that our reconstructed Voyager 2 image has a colour that is consistent with the early Voyager 2 Uranus image shown in Fig. 2a, but is less similar to a subsequently reprocessed 'true' colour image shown in Fig. 2c. This underlines the necessity of analysing all data sets with the same colour-rendering scheme in order to quantitatively compare any seasonal variations in colour.

[5]https://www.stsci.edu/hst/instrumentation/wfc3/performance/throughputs

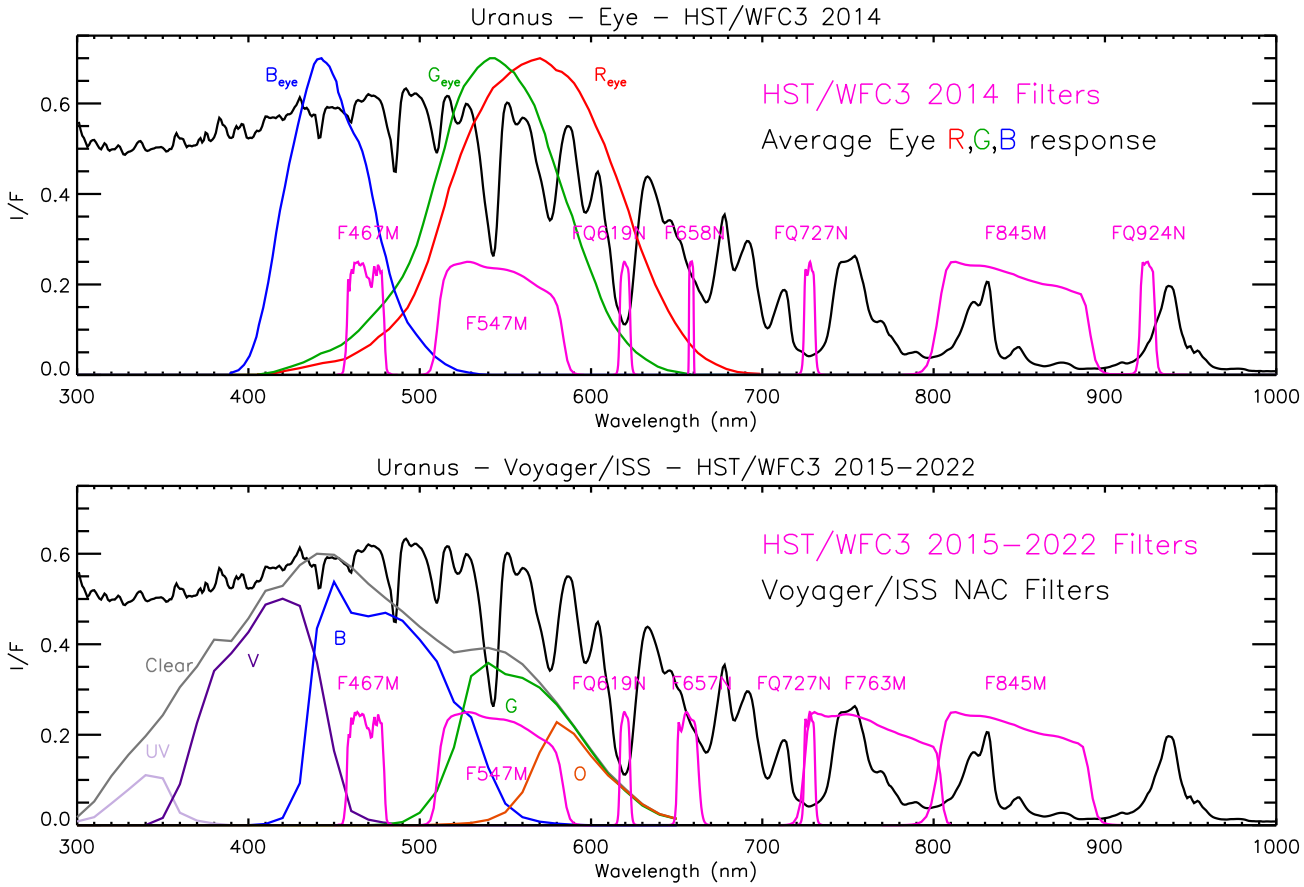

Figure 5. Average spectrum of the equatorial region of Uranus (35°S–35°N) observed in 2002 by *HST*/STIS compared with the integrated system throughputs for *HST*/WFC3 and Voyager-2/ISS Narrow Angle Camera (NAC) observations. Top panel compares the Uranus spectrum with the cone responsivities of the average human eye (e.g. R_{eye}, where the responsivities are l_{10}, m_{10}, s_{10} of Appendix A) and the *HST*/WFC3 filters (F467M, etc.) used in the 2014 OPAL observations (pink). Bottom panel compares the same Uranus spectrum with the *HST*/WFC3 filters used in the OPAL observations from 2015–2022 (pink), and also the Voyager-2/ISS NAC filter throughputs (Clear, UV, Violet, Blue, Green, Orange).

2.3 Comparison of Uranus and Neptune imaging colours

We have seen that near identically processed observations from *HST*/STIS, *HST*/WFC3, VLT/MUSE, and Voyager-2/ISS all give similar representations of the true colour of Uranus. To quantitatively determine any difference in colour between Uranus and Neptune seen by Voyager 2 in the 1980s we clearly need to analyse similarly observed Neptune observations and process these through the same pipeline. The best data available to compare against the Voyager/ISS Neptune data are the *HST*/STIS observations of Neptune made in 2003 (Karkoschka & Tomasko 2011), which were previously analysed by Irwin et al. (2022). Applying the same multiplication and integration with the XYZ colour-matching functions, transformation to sRGB followed by Gamma correction, a direct comparison of the colours of Uranus and Neptune, as seen by *HST*/STIS in 2002 and 2003, respectively, is shown in Fig. 7. Here it can be seen that although Neptune appears slightly more blue then Uranus when the intensities of both planets are scaled to their maximum, the difference in colour is not very great. Fig. 7 also shows that Neptune would appear bluer when the planet images are scaled to the correct relative size and intensity when viewed from Earth (with Uranus at 19.2 au from the Sun, and Neptune at 30.1 au), but the difference in colour is still not very strong. To understand the colours of the early Voyager images, we need to consider how the images were initially processed and compare this processing with our own pipeline.

Following on from our analysis of a set of Voyager-2/ISS Uranus observations, we applied exactly the same procedure to a set of Voyager-2/ISS Neptune approach observations (1114831: violet, 1114837: blue, 1114901: green, and 1114843: orange). Fig. 8 compares the resulting colour image of Neptune with that of Uranus (shown previously in Fig. 4), where several different processing assumptions have been applied. In row A of Fig. 8, we compare the images when the Gamma correction has not been applied and we immediately see that Neptune's disc looks much darker and bluer. Part of this relative appearance is because the images are scaled to not saturate the brightest part of the image, and for Neptune these are the bright companion clouds around the Great Dark Spot (GDS) seen on the left hand edge of Neptune. If we instead scale the intensities to not saturate the centre of Neptune's disc (row B) we already see that the disc of Neptune looks less dark and more similar to Uranus. Hence, part of the difference between the planets' colours shown in Fig. 2a and b is due to scaling the image to avoid saturating the bright-cloud regions. However, the main change in colour occurs when we apply the Gamma correction (row C) to the images, where it can be seen that the disc colours of Uranus and Neptune are now much more similar, and closer to the *HST*/STIS relative colours of Fig. 7. Going from row A (no Gamma-correction and scaled to brightest pixel) to row C (Gamma-correction) of Fig. 8 we can see that not applying the Gamma correction (row A) leads to an image with much higher

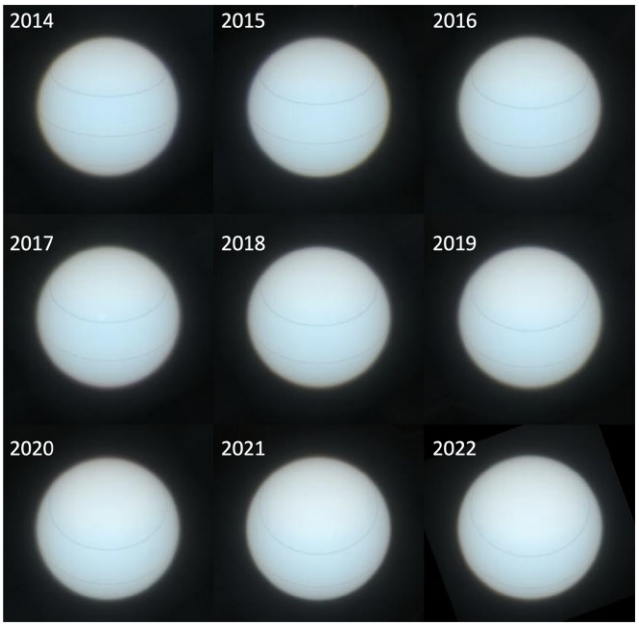

Figure 6. Reconstruction by the authors of the true visible colour of Uranus from *HST*/WFC3 OPAL observations from 2014 to 2022. Here the north pole of Uranus is at the top. As time progresses the paler north pole can be seen to swing down towards the centre and become more pronounced. Latitude lines at the equator and 35° N and S are marked for reference.

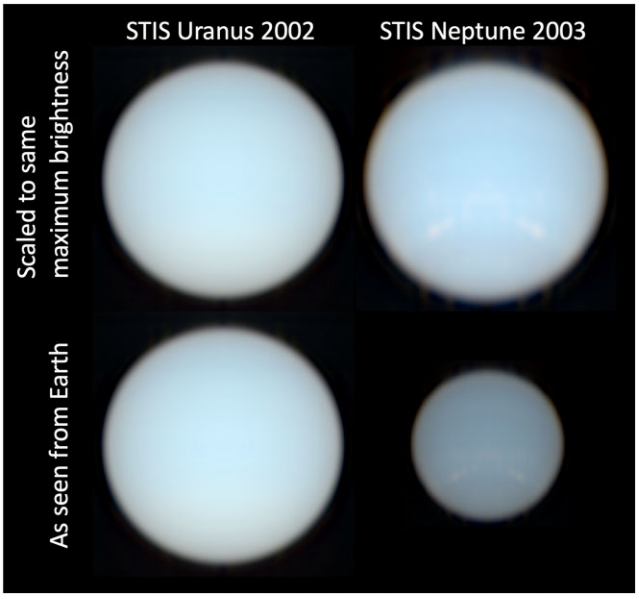

Figure 7. Reconstruction by the authors of the true visible colour of Uranus and Neptune from *HST*/STIS observations in 2002 and 2003, respectively. Top row compares planets when both are scaled to the same maximum brightness and diameter. Bottom row compares planets as seen from Earth with Neptune's disc diameter reduced and its intensity scaled by $(19.2/30.1)^2$.

contrast, which better shows the subtle distribution of dark features in Neptune's atmosphere (e.g. Smith et al. 1989), including the GDS, the South Polar Wave (SPW – the dark belt near 60°S), and Dark Spot 2 (DS2), which is embedded in the SPW and is here near the central meridian. Clearly, such features are of great interest and hence it is not surprising that the early Voyager Neptune images were contrast-

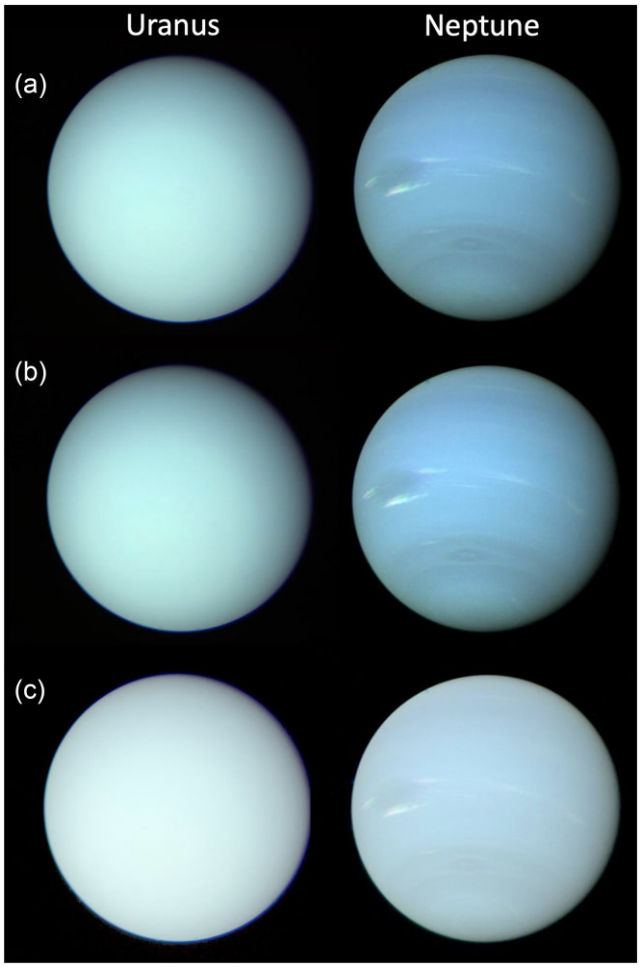

Figure 8. Reconstruction by the authors of the visible colour of Uranus and Neptune from Voyager-2/ISS NAC observations under different processing assumptions. The first row (a) compares the planets when no Gamma-correction has been applied. The middle row (b) is the same as row A, except that the Neptune image has been scaled to the centre of disc brightness, not the brightness of the brightest discrete cloud. The third row (c) compares the planets when the images have been Gamma-corrected. In this plot the south pole of Neptune is at the bottom, but the south pole of Uranus is just to the left and slightly below the centre of disc.

enhanced and not accurately coloured. Although these images were released including captions saying that there were 'enhanced' or 'stretched', these captions inevitably got separated from the images over time and have given rise to the long-standing and persistent misunderstanding of the relative colours of these two planets. We hope that this work will help make this misunderstanding more widely appreciated.

3 SEASONAL CYCLE OF URANUS'S COLOUR

Having processed the imaging observations of Uranus in a consistent way to determine their true colour, and seen how Uranus's colour has changed over the years, we now investigate what these data can tell us quantitatively about the seasonal colour changes of Uranus and compare with the Lowell Observatory long term record of disc-integrated magnitudes of Uranus in blue and green spectral filters since the 1950s (Lockwood & Jerzykiewicz 2006; Lockwood 2019).

3.1 Seasonal cycle observed with *HST*/WFC3 and *HST*/STIS data

Evidence for seasonal changes of Uranus's colour is clearly seen in the *HST*/STIS, VLT/MUSE, and *HST*/WFC3 imaging observations since 2002 shown in Section 2, with the north polar region, or polar 'hood', becoming increasingly pale and occupying a greater fraction of the observable disc (Figs 3, 4, and 6). The recent development and evolution of Uranus's polar hood is analysed by James et al. (2023), who present a detailed analysis of the observations of Uranus made with the *HST*/WFC3 OPAL observations from 2015 to 2021 and compare these with the 2012 and 2015 *HST*/STIS observations. These data are modelled with a slightly modified version of the 'holistic' cloud model of Irwin et al. (2022), where the extended deep 'Aerosol-1' layer was replaced with a vertically thin layer centred at ∼5 bar, following the development of this model for simulating VLT/MUSE observations of Neptune made in 2019 (Irwin et al. 2023a).

During the period of these *HST*/WFC3 observations, as Uranus's north pole swung towards the Sun from its equinox in 2007, the brightness of the polar regions north of ∼45°N increased in the longer wavelength channels, forming a new polar hood (Fig. 6). A corresponding south polar hood had been seen prior to Uranus's equinox surrounding the south pole (Sromovsky & Fry 2007; Karkoschka & Tomasko 2009) (visible in Fig. 3), which faded to a bright zone at ∼45°S prior to the equinox (e.g. Roman, Banfield & Gierasch 2018), while a new zone formed at ∼45°N that subsequently extended polewards (e.g. Sromovsky et al. 2009). There are several factors that could contribute towards a brighter region at Uranus's poles. First of all, the abundance of methane is known to reduce from 4–5 per cent at equatorial latitudes to 2–3 per cent at the poles (Karkoschka & Tomasko 2009) and by geometry this methane-reduced region is seen from Earth at lower zenith angles when Uranus is near solstice. Since methane is the main gaseous absorber at red and infrared wavelengths, part of the brightening can thus be explained by this methane latitudinal distribution and simple geometry. Toledo et al. (2018) analysed H-band (1.4–1.8 μm) VLT/SINFONI observations of Uranus made in 2014 and concluded that polar methane depletion was the main cause of polar brightening seen in these measurements, although a small increase in aerosol opacity was also detected. Sromovsky et al. (2019) found that a simple reduction in methane abundance at polar latitudes could not explain subsequent *HST*/STIS and Keck/NIRC2 H-band observations and that, in addition to lower methane abundances at Uranus's poles, the hood is caused by a brightening of Uranus's hazes at polar latitudes. Similarly, James et al. (2023) confirms that while part of the hood signature is due to the lower abundance of methane at polar latitudes, the reflectivity of the Aerosol-2 layer at 1–2 bar must also increase in the polar regions as the hood forms. However, the high-spectral resolution signature of the hood recovered from the *HST*/STIS data requires that the Aerosol-2 particles become more reflective only at wavelengths longer than ∼500 nm, suggesting that the scattering properties of the particles in the Aerosol-2 layer at 1–2 bar must be changing, due perhaps to compositional or size changes of the particles.

3.2 Seasonal cycle of Uranus's atmosphere determined from long-term magnitude data

The disc-integrated photometric magnitude of Uranus was observed between 1950 and 2016 by the Lowell Observatory at blue and green wavelengths, using Johnson B, V filters from 1950 to 1966, and Strömgren *b*, *y* filters from 1972 to 2016 (Lockwood & Jerzykiewicz 2006; Lockwood 2019). The Johnson B and V filters are wide-band filters centred on 420 and 530 nm, and magnitude corrections must be applied to make the data consistent with the subsequent Strömgren *b* and *y* filter observations, which are narrower filters centred on 467 and 551 nm, respectively. The filter profiles are compared in Fig. 9 with nominal spectra of Vega, the Sun, and Uranus, where the Strömgren filter profiles are from Crawford & Barnes (1970), and the Johnson filter profiles are from Bessell (1990). The magnitude system and the conversion between magnitude and equivalent planetary reflectivity are outlined in Appendix B. The offsets used to convert from Johnson B, V to Strömgren *b*, *y* magnitudes are –0.326 and 0.002, respectively (Lockwood & Jerzykiewicz 2006). The name of the Strömgren *b* and *y* filters suggests these filters observe 'blue' and 'yellow' wavelengths. However, although the central wavelength of the Strömgren *b* filter of 467 nm is well within the blue part of the spectrum, the central wavelength of the Strömgren *y* filter (551 nm) is actually green as can be seen in Fig. 10, which compares the naked eye appearance of Uranus from the *HST*/STIS 2002 data with its appearance if viewed through the Strömgren *b* or *y* filters.

The Lowell observatory data, in terms of magnitudes, are plotted in Fig. 11, with the pre-1972 estimates derived from the Johnson B, V observations indicated with different symbols from the subsequent data. Also plotted (with different symbols again) are disc-integrated magnitudes computed from the OPAL *HST*/WFC3 observations from 2014 to 2022 using the F467M and F547M filters, which are centred on the same wavelengths as Strömgren *b* and *y*, but have different widths as shown in Fig. 9. If we calculate the magnitudes expected from the reference Uranus radiance spectrum (see Appendix B) we can calculate the correction factors necessary to convert from WFC3 magnitudes to Strömgren *b* and *y* magnitudes, which are found to be +0.01 for both filters and have been applied in Fig. 11. The Lowell Observatory magnitude data, measured when Uranus was close to opposition in each year, are scaled to be those that would be measured when Uranus is 19.191 au from the Sun and 18.191 au from the Earth in order to correct for variations in these distances caused by orbital motion. Hence, the variation of magnitude with time would appear to be caused by real seasonal changes, with the Strömgren *y* magnitude varying by ∼0.1 from solstice to equinox and the Strömgren *b* changing less so. However, although referencing these magnitudes to standard distances corrects for the distance variations, it does not take into account the fact that the solid angle of Uranus's disc is larger at solstice than at equinox due to the oblateness of the planet (noted by Lockwood (2019)), which makes the equatorial radius significantly larger than the polar radius ($(R_E - R_P)/R_E = 0.023$). Overplotted in Fig. 11 are the magnitude changes expected from this oblateness factor and it can be seen that this is enough to cause most of the magnitude changes seen in the Strömgren *b* filter. However, the magnitude record does seem to indicate that Uranus is substantially greener at solstice than at equinox, as can be seen in the colour index panel of Fig. 11, which shows the difference in the Strömgren *b* and *y* magnitudes. Given our observations of the difference in colour between the polar hood of Uranus and mid-latitudes from *HST*/STIS, *HST*/WFC3, and VLT/MUSE, shown earlier, this variation in colour is to be expected since the paler polar regions will be more visible at solstice. Indeed, this seasonal variation in photometric magnitude of Uranus was known long before these Lowell observations, and records exist all the way back to the 19th Century (1870s) (Becker 1933; Alexander 1965) showing Uranus to be significantly brighter at solstice than at equinox (integrated over all visible wavelengths). One curious feature in these data is that Uranus appeared darker at both wavelengths near the 1966 equinox than near the 1985 equinox, as was noted by Hammel & Lockwood (2007). This could be interpreted as an indication of a steady slight

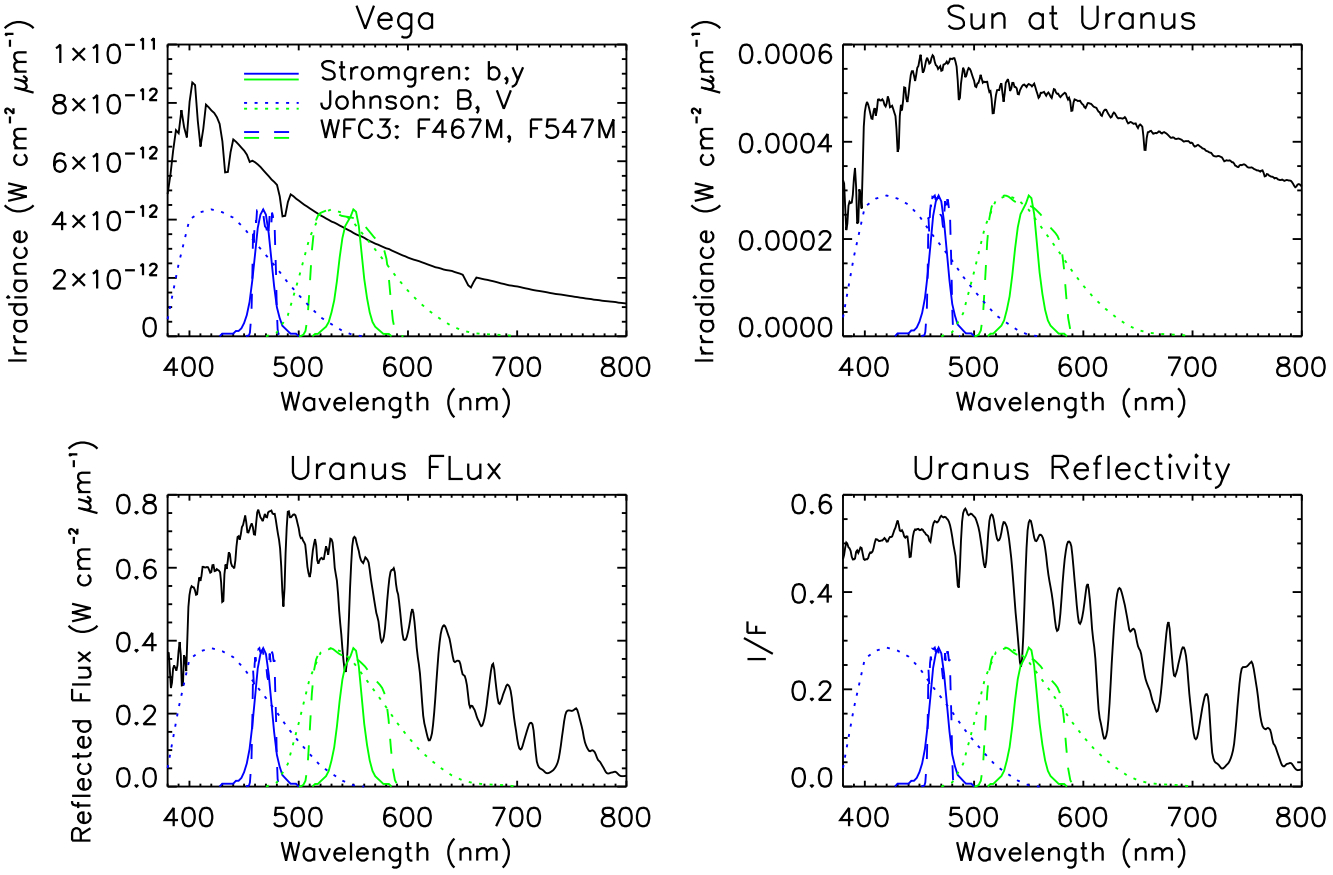

Figure 9. Spectra of Vega, Uranus, and the Sun compared with the filter transmission spectra of the Strömgren *b*, *y* filters, Johnson B, V filters, and two of the WFC3 filters (F476M, F547M). Here, the Strömgren filter profiles are from Crawford & Barnes (1970), the Johnson filter profiles are from Bessell (1990), and the WFC3 filter profiles are from the WFC3 instrument documentation (https://www.stsci.edu/hst/instrumentation/wfc3/performance/throughputs).

Figure 10. Visible appearance of Uranus reconstructed by the authors from *HST*/STIS observations in 2002 for (left) naked-eye, (centre) viewed through Strömgren *b* filter, and (right) viewed through Strömgren *y* filter.

increase in the mean reflectivity since the 1950s, although this may be partly confused by the transition between Johnson B, V to Strömgren *b*, *y* magnitudes in the early-1970s and the transition to *HST*/WFC3 magnitudes in 2016. The difference could also, however, be related to solar distance, which is shown in the bottom panel of Fig. 11, where it can be seen that the 1966 equinox occurred near Uranus's closest distance to the Sun, while the 2007 equinox occurred near Uranus's furthest distance. In addition to noting this difference in Uranus's equinox brightness, Hammel & Lockwood (2007) also noted a correlation between Neptune's brightness and solar distance, with Neptune appearing to brighten as it moved away from the Sun. It is perhaps possible that the solar distance affects the rate of formation of the dark photochemical aerosols present in Uranus's atmosphere, with a closer distance increasing the production rate and thus lowering the planetary reflectivity.

The increased brightness of Uranus at its solstices, compared to its equinoxes, is almost certainly due to the development of the polar hood of enhanced aerosol opacity in combination with the lower abundance of methane found at polar latitudes. However, multiple solutions are likely to be consistent with the measured magnitude cycles at just two colours and in order to differentiate between possible brightening scenarios we reanalysed the high-resolution 2002 *HST*/STIS observations (Karkoschka & Tomasko 2009), where polar and equatorial regions are clearly visible and separable (Fig. 3). We analysed these data using the NEMESIS radiative transfer and retrieval tool (Irwin et al. 2008) and the modified form of the 'holistic' aerosol model of Irwin et al. (2022) discussed earlier. Using the Minnaert limb-darkening approximation (Minnaert 1941), introduced earlier (equation (2)), we determined the Minnaert coefficient spectra of nadir reflectivity $(I/F)_0$ and limb-darkening coefficient k for two regions on the planet (1) equatorial latitudes from 35°S to 35°N and (2) polar latitudes south of 45°S. Significantly different $(I/F)_0$ and k spectra were found for these two regions and the differences between these spectra are shown in Fig. 12. To interpret these spectral differences, we first retrieved a model atmosphere from the equatorial $(I/F)_0$ and k spectra using the method of Irwin et al. (2022), that is, simultaneously fitting the modified 'holistic' model to two synthetic observation spectra generated from the Minnaert coefficients at 0° and 61.45° zenith angles for both incident and reflected beams in the back-scatter

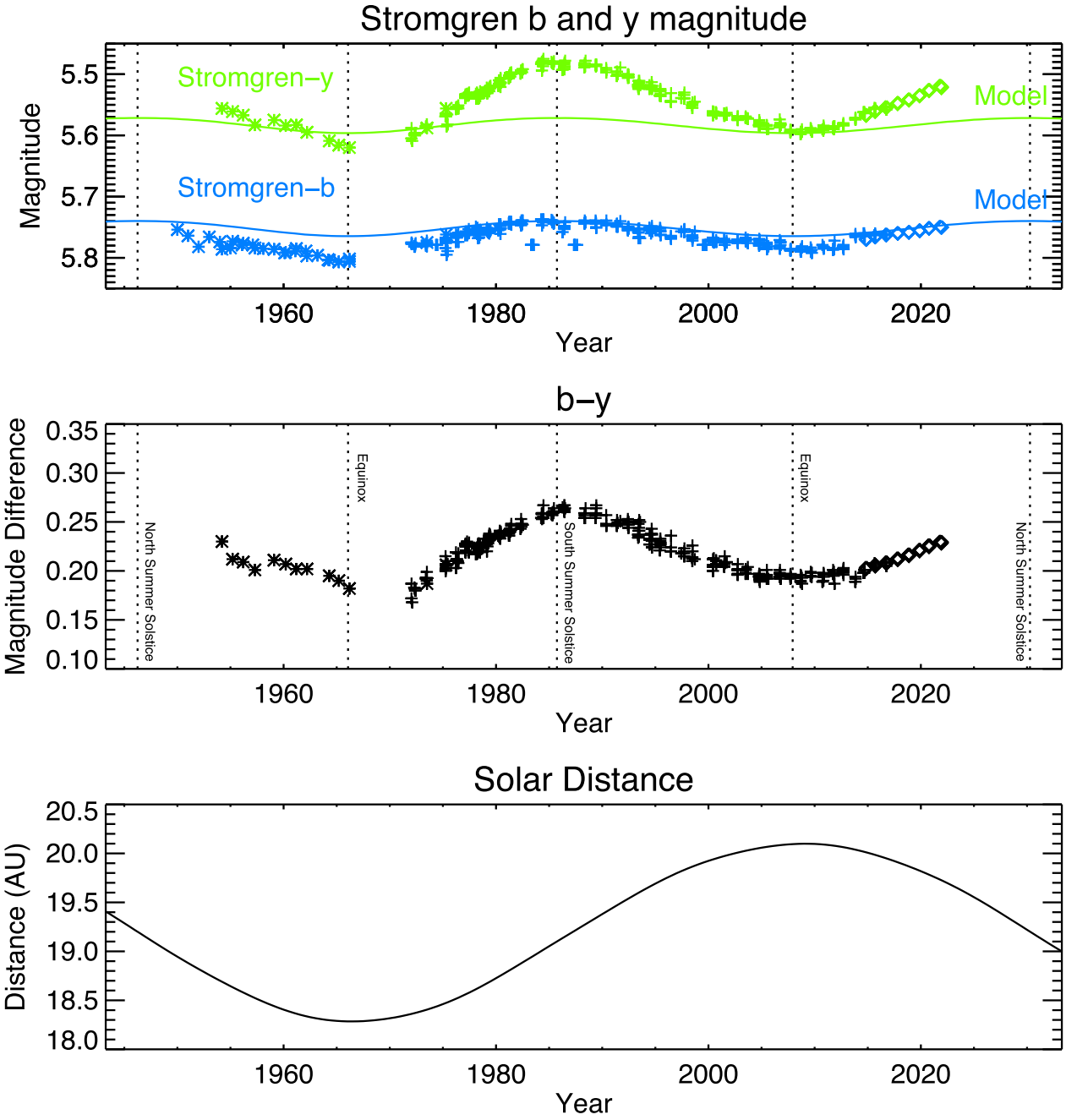

Figure 11. Top panel: Long term record of Strömgren *b* and *y* magnitudes of Uranus (scaled to constant distances from the Sun and Earth of 18.191 and 19.191 au, respectively). Estimates from the Lowell Observatory (Lockwood & Jerzykiewicz 2006; Lockwood 2019) were recorded directly in these Strömgren filters from 1972–2016 (crosses) or converted from Johnson B and V observations from 1950–1966 (asterisks). Also shown are the equivalent Strömgren magnitudes computed from OPAL *HST*/WFC3 observations in the F467M and F547M filters from 2014–2022 (diamonds). Overplotted are NEMESIS-simulated seasonal magnitude curves for Uranus in these filters (solid coloured lines) modelled with fixed methane abundance and aerosol opacity at all points on Uranus's disc and thus only simulating the effect of changes in Uranus's projected disc size during its orbit caused by its oblateness, with a larger disc and thus increased brightness seen at solstices. The positions of the equinoxes and solstices are marked with the vertical dotted lines. Middle panel: Variation in Strömgren $b - y$ colour index with time, showing Uranus to be greener at solstice, and bluer at equinox. Bottom panel: Distance of Uranus from the Sun in astronomical units (au).

direction, that is, $\mu = \mu_0$, with the Minnaert relation reducing to $I/F = (I/F)_0 \mu^{2k-1}$. Having fitted the aerosol opacities, Aerosol-2 base pressure, methane abundance, and complex refractive index spectra of the particles to the equatorial spectra, we then adjusted the model parameters in turn to see what effect these changes would have on the simulated reflectance spectra. The differences in the modelled $(I/F)_0$ and k spectra are compared with the observed pole–equator differences in Fig. 12, where the difference in $(I/F)_0$ is simply $(I/F)_{0\mathrm{Adj}} - (I/F)_{0\mathrm{Ref}}$ and the difference in k is $k_{\mathrm{Adj}} - k_{\mathrm{Ref}}$, where 'Ref' is the reference model fitted to the equatorial data and 'Adj' are the perturbed, or adjusted models. Here, the modelled $(I/F)_0$ spectra are simply the forward-modelled nadir spectra (i.e. $\mu = 1$), while the

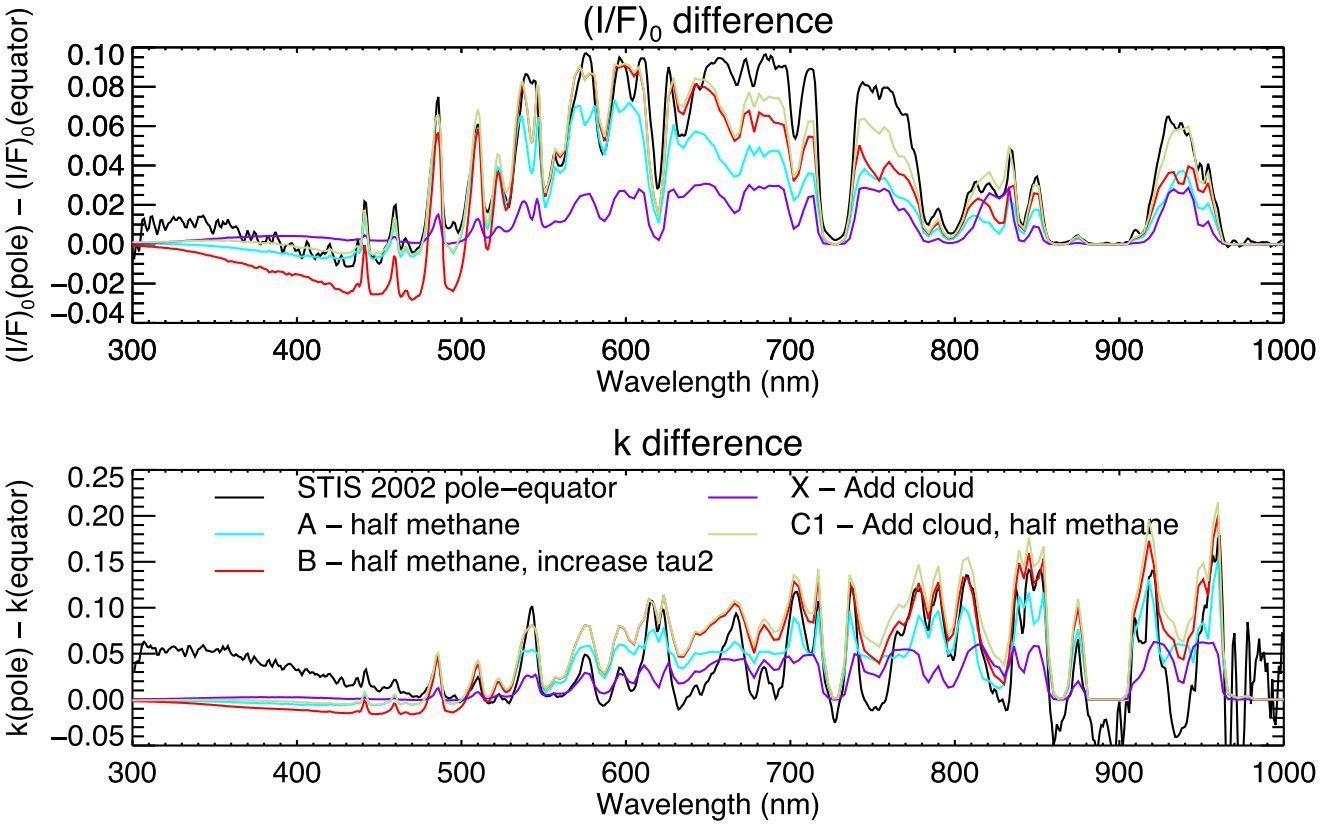

Figure 12. Comparison of the differences between the fitted Minnaert nadir $(I/F)_0$ and limb-darkening k spectra at polar and equatorial latitudes from *HST*/STIS 2002 observations, compared with modelled differences caused by changing the atmospheric model as described in the text.

modelled limb-darkening spectra k are calculated from the forward-modelled spectra at nadir and 61.45° zenith angle using

$$k = 0.5 \times \left(1 + \frac{\log(I/F)_\mu / \log(I/F)_0}{\log \mu}\right), \quad (3)$$

where $(I/F)_0$ is the modelled nadir spectrum, $(I/F)_\mu$ is the modelled spectrum at 61.45°, and $\mu = \cos(61.45°)$.

First, we halved the deep methane abundance (model A), since we know the polar regions are methane-depleted, but found that although such a change produces changes in $(I/F)_0$ and k that reasonably approximate the shape of observed differences between the polar and equatorial regions in Fig. 12, the amplitude is not sufficiently large and is close to zero at blue wavelengths. Secondly, we tried halving the methane abundance and increasing the opacity of the Aerosol-2 layer, τ_2, by 1.0 (model B), from 4.6 to 5.6. Note that all opacities quoted here are at a reference wavelength of 800 nm. Here, we see an increase in the $(I/F)_0$ and k difference at green wavelengths, but a decrease at blue wavelengths. The reason for this is that the Aerosol-2 particles are retrieved to have increased imaginary refractive index at blue wavelengths (Irwin et al. 2022), which lowers the single-scattering albedo here. Hence, increasing the Aerosol-2 opacity reduces the reflectivity at blue wavelengths, rather than increasing it. How then can we match the observed differences between the polar and equatorial spectra of the 2002 *HST*/STIS data? In the study of James et al. (2023), noted earlier, it was found that the optimal solution was to not only increase the opacity of the particles in the Aerosol-2 layer, but also make them more reflective at wavelengths longer than 500 nm. We could have similarly adjusted the imaginary refractive index spectra, $n_{\rm imag}$, of the Aerosol-2 particles (lower $n_{\rm imag}$ values increase the single-scattering albedo), but in a parallel analysis of VLT/MUSE observations of Neptune, Irwin et al. (2023b) found that the observed spectra of deep bright spots could be well approximated by adding a component of bright particles to the existing Aerosol-1 layer at ∼5 bar. We wondered whether a similar approach might be applicable here. Changes in the Aerosol-1 layer cannot account for the observed *HST*/STIS pole–equator differences, since this layer is only detectable in narrow wavelength bands of very low methane absorption, but in Fig. 12 it can be seen that if we add a unit opacity of conservatively scattering particles to the Aerosol-2 layer at 1–2 bar (with the same Gamma size distribution as the Aerosol-2 particles, with mean radius 0.6 μm and variance σ = 0.3) the $(I/F)_0$ and k difference increases at all wavelengths longer than ∼ 480 nm (model X), although not as much as the difference between polar and equatorial latitudes. However, if we add this additional opacity *and* simultaneously halve the methane abundance (Model C1) we find that the differences in the $(I/F)_0$ and k spectra agree moderately well with the observed pole–equator difference spectra at most wavelengths. What might be responsible for this extra component of bright particles in the Aerosol-2 layer will be discussed further, but it could indicate that more methane ice particles are present in the haze/methane-ice layer, or that more methane ice is condensed onto the haze Cloud Condensation Nuclei (CCN). Whatever the cause, it is clear that the spectral difference between the polar and equatorial regions seen by *HST*/STIS in 2002 is consistent with a reduction in methane abundance coupled with an increase in the reflectivity of the particles in the Aerosol-2 layer that could be caused by the addition of a conservatively scattering component.

Having surveyed the possible interpretations of the *HST*/STIS polar and equatorial spectra, we then tested these models against the

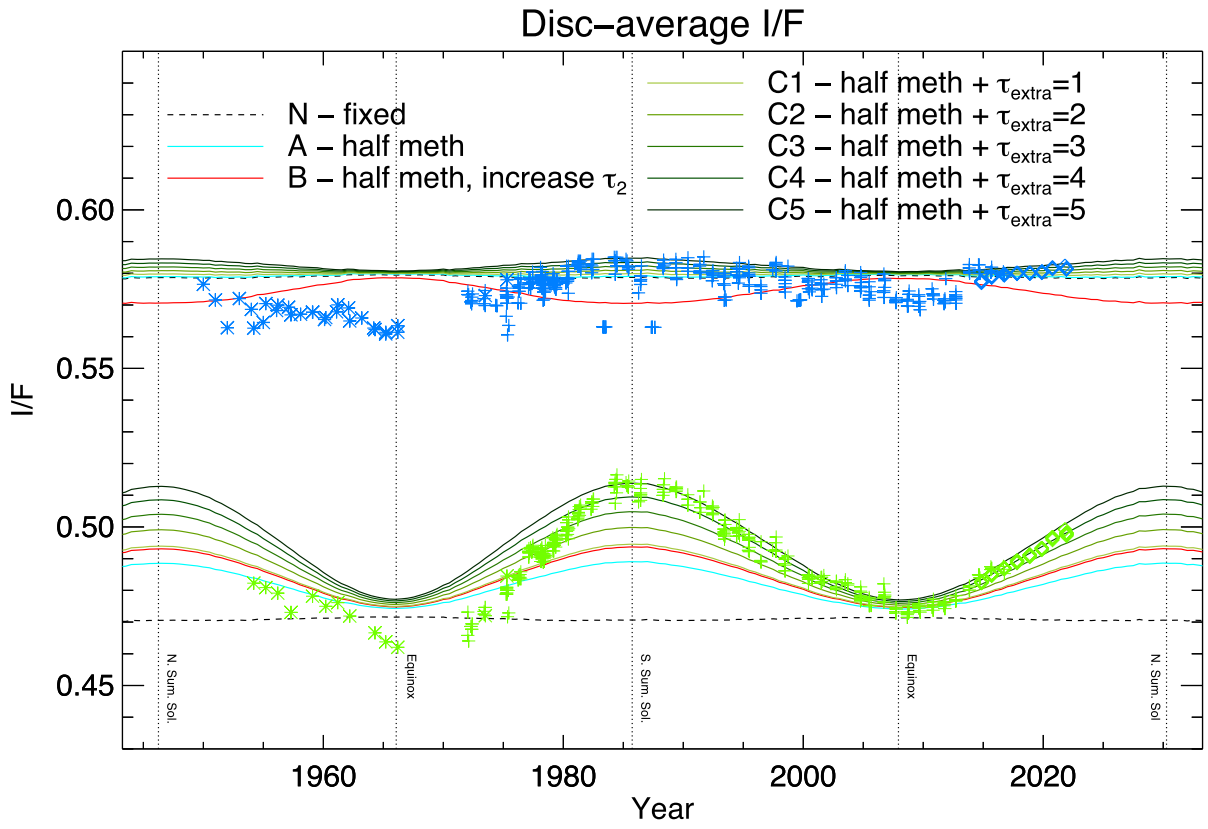

Figure 13. Long term magnitude data of Uranus from 1950 to 2022 at Strömgren *b* and *y* wavelengths, previously shown in Fig. 11, but here converted to equivalent disc-averaged reflectivities following the procedures outlined in Appendix B. Seasonal curve computations from our NEMESIS radiative transfer model are also shown, which are described more fully in the main text. Models are (N) equatorial conditions at all locations; (A) polar methane (i.e. polewards of 40°) halved; (B) polar methane halved and Aerosol-2 opacity increased by $\tau = 1$; (C) polar methane halved and conservatively scattering particles added to Aerosol-2 with opacity of $\tau = 1$ to $\tau = 5$. All cloud opacities are quoted at 800 nm.

seasonal photometric magnitude data. While the Lowell Observatory magnitude data accurately preserve the quantities that were measured, they are a less intuitive measure for interpreting the changes in Uranus's reflectivity spectrum with atmospheric models. Hence, we converted the magnitudes to the mean disc-averaged reflectivities of Uranus, which also corrects out the solid-angle variations of Uranus's disc size, noted earlier. This conversion was done using the procedures outlined in Appendix B. The resulting seasonal variations in disc-averaged reflectivity at the blue and green wavelengths of the Strömgren *b* and *y* filters are shown in Fig. 13. Here, it can be seen that the disc-averaged green reflectivity of Uranus changes from ∼0.47 to ∼0.51 from equinox to solstice, while the disc-averaged blue reflectivity changes much less with a peak-to-peak change in reflectivity of ∼0.02. As noted earlier, for both colours there is an indication of a steady slight increase in the mean reflectivity since the 1950s, which may be partly confused by the transition between different data sets, but might also be dependent on Uranus's distance from the Sun. What does seem to be clear, however, is that the reflectivity increased more rapidly to its maximum at the 1985 solstice and decayed more slowly after, with the new increase in reflectivity to the 2030 solstice increasing at a similar rate to that seen between 1972 and 1986. However, we should note that the eccentricity of Uranus's orbit means that although 19.67 yr elapsed between Uranus's southern summer equinox in January 1966 and its southern solstice in September 1985, 22.19 yr elapsed between the southern solstice and the northern spring equinox in December 2007, nearly 3 yr longer, which partly explains this difference in gradient. There is other evidence, though, of possible asymmetries in the seasonal brightening and fading of the polar hood. During the approach to Uranus's equinox in 2007 the south polar hood retreated into a circumpolar zone at ∼45°S, while an analogous zone appeared at ∼45°N, which subsequently extended to the north pole, as noted earlier. However, while the south polar hood was clearly visible in 2002 *HST*/STIS observations, 5 yr before equinox, the north polar hood was less visible in 2012 *HST*/STIS observations, 5 yr after equinox, suggesting that the hood/circumpolar-zone decays more slowly than it forms. The north polar hood has since been seen to be brightening rapidly in the *HST*/WFC3 observations analysed by James et al. (2023) and also presented here.

Fig. 13 compares the observed mean reflectivities in the Strömgren *b* and *y* filters with predictions computed with our NEMESIS atmospheric models of the equatorial and polar regions observed by *HST*/STIS in 2002 and shown in Fig. 12. For each point in Uranus's seasonal cycle around the Sun, the distribution of zenith angles and latitude across the disc at opposition were computed using geometry and ephemeris data from JPL Horizons.[6] Then at each point on the disc the expected spectra from the equatorial fit and possible polar perturbations were computed from the Minnaert coefficients at the local zenith angles and then combined as

$$(I/F) = (1 - f)(I/F)_{Ref} + f(I/F)_{Adj}, \quad (4)$$

[6]https://ssd.jpl.nasa.gov/horizons

where the weighting factor f was assumed to vary with latitude ϕ (in degrees) as

$$f = (1 + \tanh(10\pi(|\phi| - 40.0)/180.))/2. \quad (5)$$

This distribution gives $f = 0$ at the equator and $f = 1$ at the poles, with a cross-over latitude of 40°.

In the first simulation (model N), the polar regions were set to have the same atmospheric properties, and thus scattering behaviour, as the equatorial regions, and it can be seen that the variation in mean reflectance is negligible, as expected. The small variations remaining are due to slight seasonal variations in the relative weights between the limb and nadir spectra due to Uranus's oblateness. If we set the polar regions to have half the methane abundance of the equator (i.e. model A), then we find the reflectivity at both wavelengths changes with the right sign, but that the amplitude of the variations in Strömgren *y* filter is smaller than that observed. Hence, the conclusion of Toledo et al. (2018) that the hood at H-band wavelengths is mainly caused by a lower methane abundance at the poles, is not consistent with observations at shorter wavelengths, where the scattering opacity of small particles is more significant, as noted by Sromovsky et al. (2019) and James et al. (2023). If we both halve the methane abundance and increase the opacity of the Aerosol-2 particles in the polar region by 1.0 at 800 nm (model B), we find that we get an improved correspondence to the measured reflectivities at Strömgren *y*, but again completely the wrong behaviour at Strömgren *b*, with the reflectivity being lowest at the solstices, not highest. As before, this is due to the lower single-scattering albedo of the modelled Aerosol-2 particles at blue wavelengths. However, in models C1 – C5 we both halve the methane abundance at the poles and add progressively more opacity of conservatively scattering particles to the Aerosol-2 layer, which leads to a good correspondence with the measured reflectivities at both wavelengths for additional opacities of 3–5 at 800 nm (compared with the fitted Aerosol-2 opacity at equatorial latitudes of 4.6). The reason that adding scattering particles to Aerosol-2 has a large effect on the Strömgren *y* reflectivities, but little effect at Strömgren *b* wavelengths, is because at the pressure of the Aerosol-2 layer (1–2 bar) the Rayleigh scattering from the surrounding air is already substantial at blue wavelengths. Hence, adding more highly scattering particles does not increase the reflectivity very much.

It is notable that while we achieve a reasonably good fit to the data from the late-1970s onwards with models C1–C5, agreement with the earlier data is not as good. As noted earlier, this may be partly due to inaccuracies in converting Johnson B, V magnitudes to Strömgren *b*, *y*, but it might also be due to a steady apparent increase in the brightness of Uranus since 1950 at both wavelengths. Alternatively, we have assumed here that the scattering properties of the equatorial regions of Uranus remain constant with time, but as noted earlier it perhaps may be the case that the reflectivity of these regions changes depending on Uranus's distance from the Sun. When Uranus was closest to the Sun in 1966 the photochemical production rate of dark haze particles would have been at its highest, and these are thought to be combined with methane ice in the Aerosol-2 layer at 1–2 bar (Irwin et al. 2022). A higher proportion of dark haze particles in 1966 may have made the equatorial regions darker than they were at the next equinox in 2007, when Uranus was near its furthest point from the Sun and photochemical production rates were at their lowest.

4 DISCUSSION

As noted in the introduction, the seasonal variation in the properties of Uranus's polar hood has been studied for decades since the Voyager 2 encounter in 1986. Previous studies (Rages, Hammel & Friedson 2004; Sromovsky & Fry 2008; Toledo et al. 2018; Sromovsky et al. 2019; James et al. 2023) all concur that the hood is likely caused by an increase in the reflectivity of the aerosols near 1–2 bar, combined with reduced methane abundance in the polar regions. In this study we find that adding a component of highly scattering particles to the Aerosol-2 layer at 1–2 bar (presumed to be a mixture of haze and CH_4 ice) at polar latitudes, combined with the polar reduction in deep methane abundance, has the required spectroscopic signature to match *HST*/STIS observations and is also able to reproduce well the seasonal cycles of Uranus's brightness at blue and green wavelengths recorded by Lowell Observatory (Lockwood & Jerzykiewicz 2006; Lockwood 2019). A similar scenario has been proposed by Irwin et al. (2023b) to account for reflectivity changes seen in Neptune's atmosphere in narrow wavelength bands longer than 650 nm, but here the changes are in the deeper Aerosol-1 layer at ∼5 bar (presumed to be a mixture of haze and H_2S ice). In both cases it may be that additional bright ice particles are condensing at these respective levels and for Uranus's polar hood it may be that the increased solar heating of the polar regions causes the air to become even more stable, which will reduce the rate at which the Aerosol-2 layer is removed by methane 'snow' at its base and perhaps lead to a higher fraction of smaller methane ice particles in that layer. This is very similar to mechanism proposed by Irwin et al. (2022) to explain why the Aerosol-2 layer on Uranus is twice as thick as that on Neptune (giving Uranus its paler colour), with more vigorous convection in Neptune's atmosphere mixing deep methane more efficiently up to the condensation level, where it can condense on the accumulating haze particles and remove them. However, Orton et al. (2015) and Roman et al. (2020) note no significant changes in Uranus's tropospheric temperatures from Voyager to equinox and beyond.

As time has elapsed since the Voyager 2 encounter, Uranus is now approaching a similar point in its northern summer as the point in the southern summer seen by Voyager 2 in 1986. It will thus be of great interest to see how closely the observations that may be made up to, and through, 2031 will correspond with the Voyager 2 observations of 1986. Although Uranus's atmospheric features are generally subtle, there is actually significant latitudinal variation in the Voyager 2 ISS observations (e.g. Karkoschka 2015). Smith et al. (1986) presents an overview of these observations, including images of Uranus that have been divided by the expected reflectances from a Minnaert model to enhance the subtle spatial variations seen. In a similar vein, taking our modified 'holistic' model fit to the *HST*/STIS 2002 disc-averaged data, we simulated the expected Voyager-2/ISS NAC images of Uranus and divided the observed images by these synthetic images to yield the enhanced disc images shown in Fig. 14, for a set of observations made during Voyager 2's approach. As can be seen the polar hood is clearly visible in the NAC images at green and orange wavelengths, but at shorter wavelengths, the polar region becomes darker than expected, especially near the pole in the blue image. In addition, it can be seen that the hood at green and orange wavelengths looks brightest at its edge at ∼45°S, but becomes less bright towards the pole.

What causes these features, and might similar features become visible in the current *HST*/WFC3 observations being made as we approach the next solstice? To start to answer this, we took the latest set of *HST*/WFC3 observations from 2022 and again divided these by the expected synthetic images calculated from our best fit disc-average model to yield the enhanced disc images shown in Fig. 15. The wavelengths observed by *HST*/WFC3 are mostly much longer than the Voyager-ISS/NAC filters, or in regions of strong methane

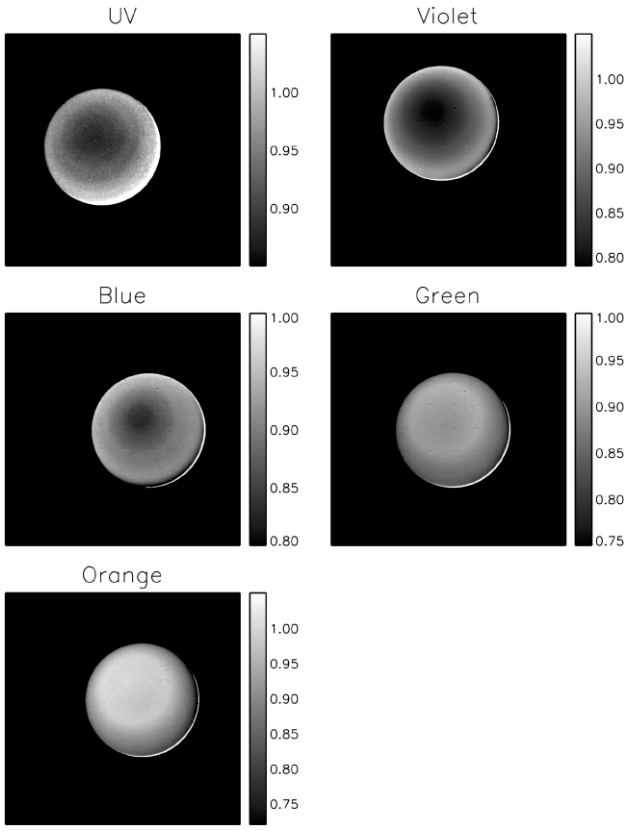

Figure 14. Voyager 2 ISS/NAC observations of Uranus in 1986 in various filters, divided by the expected disc appearance from our modified disc-averaged 'holistic' model of the 2002 *HST*/STIS observations to accentuate latitudinal variations. Observation IDs are 2652251: UV, 2651528: violet, 2651307: blue, 2651510: green, 2651313: orange. The ratio of true/modelled images is indicated by the associated grey-scale bar.

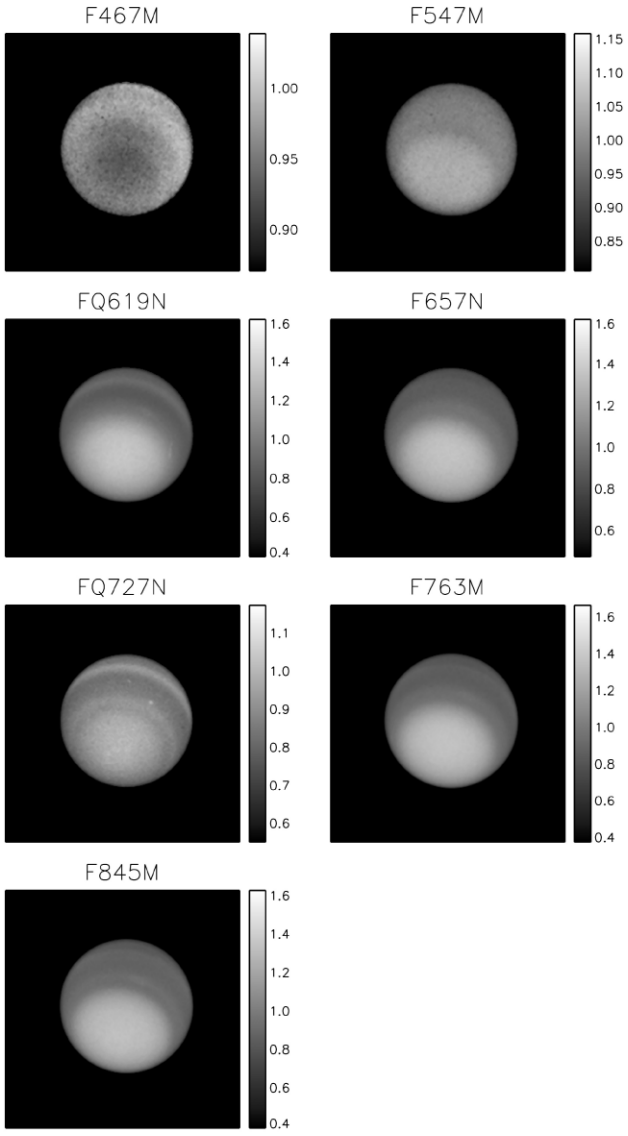

Figure 15. *HST*/WFC3 observations of Uranus in 2021 in various filters, divided by the expected disc appearance from our modified disc-averaged 'holistic' model of the 2002 *HST*/STIS observations to accentuate latitudinal variations. The ratio of true/modelled images is indicated by the associated grey-scale bar. The central wavelength of each filter is given in the filter name. Hence, for example, the F845M filter is centred at 845 nm.

absorption, so it is hard to compare like with like. However, a clear hood is seen in all filters longer than F467M, with no apparent dimming towards the pole yet visible. Interestingly, in the F467M filter, whose central wavelength is close to that of the Voyager 2 NAC blue filter, we see a very slight darkening of the polar regions. Could such a darkening perhaps be due to an increase in the opacity of the background Aerosol-2 particles at these wavelengths, or an increase in their absorption? Or might it be due to changes in the underlying Aerosol-1 layer? It is difficult to differentiate between such scenarios with filter images like this, which underlines the need to continue to monitor the current seasonal development of the north polar hood with spectral imaging instruments such as *HST*/STIS or VLT/MUSE, which can differentiate between different possible scenarios. *HST*/STIS observations would be preferable due to its wider wavelength coverage (extending to 300 nm in contrast to MUSE's lower limit of 473 nm) and no terrestrial atmospheric effects to correct for. A preliminary analysis of the shortest wavelength slices of the 2021 MUSE cube (473–483 nm) reveal no polar darkening at blue wavelengths yet, but these wavelengths are at the limit of MUSE's sensitivity. It will be very interesting to see if a dark region forms about Uranus's north pole at blue wavelengths as we move towards solstice in 2030, and also whether the hood dims slightly polewards of 45°N at longer wavelengths. These changes should be detectable with the ongoing OPAL *HST*/WFC3 Uranus programme.

Finally, we are fortunate indeed to have long-time series data set from the Lowell Observatory from 1950–2016 to investigate these changes in Uranus's seasons, but the historical record of observations of Uranus's brightness extends much further back to to the middle of the 19th Century (e.g. Becker 1933; Alexander 1965), revealing a long-standing and regular increase of Uranus's brightness at its solstices. Historical imaging observations also exist, extending back to the beginning of the 20th Century, with sketches of Uranus's visual appearance to the Grand Lunette at the Observatoire de Paris – Meudon in 1924, near equinox, and expectations of its appearance near its solstice bearing a remarkable similarity with more modern imaging data (Fig. 16).

5 CONCLUSIONS

In this study we have presented a detailed quantitative analysis of the seasonal record of Uranus's photometric magnitude at blue

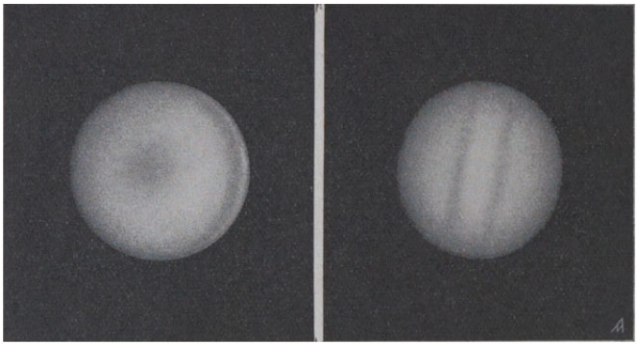

Figure 16. Right: Sketch of visual observations of Uranus made in 1924 near equinox from the Observatoire de Paris – Meudon Grand Lunette. On the left is shown an expectation of Uranus's appearance near the following solstice. Reproduction of figs. 149 and 150 of Antoniadi (1936), also reviewed by Alexander (1965).

and green wavelengths (Strömgren *b* and *y* filters), recorded at the Lowell Observatory from 1950 to 2016 (Lockwood & Jerzykiewicz 2006; Lockwood 2019). We have compared these measurements with filter-imaging and spectral-imaging observations of Uranus and Neptune to reproduce, as accurately as possible, the true visible colour of these planets, and how Uranus's colour changes with time. We have used these data to constrain models of the 'hood' of haze that develops over the summer pole of Uranus as the planet heads towards solstice and then subsequently decays, to be replaced by an equivalent hood at the other pole. Our main conclusions are:

(i) We find that the seasonal variations of Uranus's reflectivity at blue and green wavelengths (Strömgren *b* and *y* filters) can be explained by the lower abundance of methane at polar latitudes combined with an increase in the reflectivity at longer wavelengths of the aerosol particles near the methane condensation level at 1–2 bar (i.e. Aerosol-2 of of the 'holistic' model of Irwin et al. 2022). This increase in reflectivity is consistent with the addition of conservatively scattering particles to this layer, for which the background particles are found to be strongly absorbing at both blue and red wavelengths. We suggest that this additional component may come from a higher proportion of methane ice particles, perhaps due to the stabilizing effects of spring and summer sunlight on the tropospheric temperature field, although no significant changes in Uranus's tropospheric temperatures since the Voyager 2 flyby have yet been detected (Orton et al. 2015; Roman et al. 2020).

(ii) The Lowell magnitude data reveal an apparently steady increase in reflectivity of Uranus since the 1950s at both blue and green wavelengths. This could be an artefact of the data, or perhaps be caused by long term changes in Uranus's climate, but we note here that there could also be dependence on Uranus's distance from the Sun, which will affect the production rate of dark photochemical haze. This production rate would be highest when Uranus is closest to the Sun, which corresponds with the generally lower reflectivities seen at this time.

(iii) Although the background atmospheres of Uranus and Neptune (i.e. away from discrete bright clouds) are differently coloured, due to the increased thickness on Uranus of a layer of aerosol near the methane condensation level at 1–2 bar (i.e. Aerosol-2), and although the colour of Uranus changes seasonally as just described, the difference in colour between Uranus and Neptune is much less distinct than is seen in the colour images released immediately after the Voyager 2 flybys of Uranus in 1986, and Neptune in 1989. This is because the Neptune images were contrast-enhanced to accentuate faint, dark features and are not 'true' colour. However, although this fact has been noted by several previous authors, this commonly held misperception remains persistent.

(iv) We find that the conversion of filter-imaging observations to 'true' colour is a surprisingly subtle process and requires detailed understanding of the underlying Uranus and Neptune spectra, and also how the Gamma correction is used to encode and then correct for image intensities. Applying the same processing to Voyager-2/ISS and subsequent imaging data sets we find much more similarity between the 'true' colours of Uranus and Neptune and how the colour or Uranus changes with time.

A parallel study of *HST*/STIS and *HST*/WFC3 observations by James et al. (2023) comes to similar conclusions concerning the nature of Uranus's polar hood, but also retrieves the latitudinal distribution of aerosol and methane abundance. Although filter-imaging observations cannot constrain the methane abundance (methane retrievals require spectral measurements from 800–860 nm, where hydrogen–helium collision-induced absorption can be used to disentangle haze from methane abundance), the Voyager 2 ISS filter-imaging observations of Uranus have both remarkable similarities with, and differences from, the *HST*/WFC3 observations currently undertaken annually as part of the OPAL programme (Simon, Wong & Orton 2015). As Uranus heads towards its northern summer solstice in 2030 we expect Uranus's northern polar hood to become more and more like that seen by Voyager 2 ISS in 1986. However, to compare more directly with the earlier Voyager 2 ISS observations, we recommend that the future Hubble observations include filters that correlate better with the filters used by Voyager-2/ISS, especially at shorter wavelengths. In addition, we recommend that spectral imaging of Uranus continues with instruments such as *HST*/STIS and VLT/MUSE, which can estimate the latitudinal distribution of methane and retrieve more robust cloud profiles and scattering properties.

ACKNOWLEDGEMENTS

We are grateful to the United Kingdom Science and Technology Facilities Council for funding this research (PGJI: ST/S000461/1, NAT: ST/R000980/1). GO was supported by funding to the Jet Propulsion Laboratory, California Institute of Technology, under a contract with the National Aeronautics and Space Administration (80NM0018D0004). LF and MR were supported by a European Research Council Consolidator Grant (under the European Union's Horizon 2020 research and innovation programme, grant agreement no. 723890) at the University of Leicester. SP-H is supported by grant number PID2019-109467GB-I00Z, funded by MCIN/670 AEI10.13039/501100011033 and Elkartek KK-2023/00077. This review includes observations made with the NASA/ESA *Hubble Space Telescope* obtained from the Space Telescope Science Institute, which is operated by the Association of Universities for Research in Astronomy, Inc. (AURA), under NASA contract number NAS 5–26555. These observations are associated with STIS programme(s) GO9035, GO9330, GO12894, GO14113, and WFC3 programmes GO13937, GO14334, GO14756, GO15262, GO15502, GO15929, GO16266, GO16790, GO16995. AS is supported by grants from the Space Telescope Science Institute associated with programme GO13937. We would also like to express our gratitude to Björn

Jónsson for his helpful advice on colour rendering and finally, we would like to thank our reviewer, Heidi Hammel, for her very helpful and constructive feedback, and also for clarifying how the issue of 'true' colour was debated amongst the Voyager imaging team during the 1980s.

6 DATA AVAILABILITY

The data underlying this article will be shared on reasonable request to the corresponding author. Please note, however, that the Hubble data are publicly available at the Mikulski Archive for Space Telescopes (https://mast.stsci.edu/) under the programme numbers listed in the acknowledgements.

REFERENCES

Adel A., Slipher V. M., 1934, Nature, 134, 148
Alexander A. F. O., 1965, The planet Uranus; a history of observation, theory, and discovery. Faber and Faber, London
Antoniadi E. M., 1936, L'Astronomie, 50, 249
Aplin K. L., Harrison R. G., 2016, Nature Communications, 7, 11976
Aplin K. L., Harrison R. G., 2017, Geophys. Res. Lett., 44, 12,083
Atreya S. K., Hofstadter M. H., In J. H., Mousis O., Reh K., Wong M. H., 2020, Space Sci. Rev., 216, 18
Becker W., 1933, Sitzungsberichte der Preussischen Akademie, 28, 849
Bessell M. S., 1990, PASP, 102, 1181
Chance K., Kurucz R. L., 2010, J. Quant. Spec. Radiat. Transf., 111 , 1289
Chavez E., et al., 2023, Icarus, 404, 115667
Colina L., Bohlin R., Castelli F., 1996, STScI, Instrument Science Report CAL/SCS-008
Crawford D. L., Barnes J. V., 1970, AJ, 75, 978
Danielson G. E., Kupferman P. N., Johnson T. V., Soderblom L. A., 1981, J. Geophys. Res., 86, 8683
Hammel H. B., Lockwood G. W., 2007, Icarus, 186, 291
Irwin P. G. J., et al., 2008, J. Quant. Spec. Radiat. Transf., 109, 1136
Irwin P. G. J., et al., 2022, J. Geophys. Res.:Planets, 127, e07189
Irwin P. G. J., et al., 2023a, Nat. Astron., 7, 1198
Irwin P. G. J., et al., 2023b, J. Geophys. Res.:Planets, 128, e07980
James A., et al., 2023, J. Geophys. Res.:Planets, 128, e07904
Karkoschka E., 2015, Icarus, 250, 294
Karkoschka E., Tomasko M., 2009, Icarus, 202, 287
Karkoschka E., Tomasko M. G., 2010, Icarus, 205, 674
Karkoschka E., Tomasko M. G., 2011, Icarus, 211, 780
Lockwood G. W., 2019, Icarus, 324, 77
Lockwood G. W., Jerzykiewicz M., 2006, Icarus, 180, 442
Lockwood G. W., Thompson D. T., 2002, Icarus, 156, 37
Minnaert M., 1941, ApJ, 93, L403
Orton G. S., Fletcher L. N., Encrenaz T., Leyrat C., Roe H. G., Fujiyoshi T., Pantin E., 2015, Icarus, 260, 94
Rages K. A., Hammel H. B., Friedson A. J., 2004, Icarus, 172, 548
Roman M. T., Banfield D., Gierasch P. J., 2018, Icarus, 310, 54
Roman M. T., Fletcher L. N., Orton G. S., Rowe-Gurney N., Irwin P. G. J., 2020, AJ, 159, 45
Roman M. T., et al., 2022, Plan. Space. J., 3, 78
Simon A. A., Wong M. H., Orton G. S., 2015, ApJ, 812, L55
Smith B. A., et al., 1986, Science, 233, 43
Smith B. A., et al., 1989, Science, 246, 1422
Sromovsky L. A., Fry P. M., 2007, Icarus, 192, 527
Sromovsky L. A., Fry P. M., 2008, Icarus, 193, 252
Sromovsky L. A., Fry P. M., Hammel H. B., Ahue W. M., de Pater I., Rages K. A., Showalter M. R., van Dam M. A., 2009, Icarus, 203, 265
Sromovsky L. A., Karkoschka E., Fry P. M., Hammel H. B., de Pater I., Rages K., 2014, Icarus, 238, 137
Sromovsky L. A., Karkoschka E., Fry P. M., de Pater I., Hammel H. B., 2019, Icarus, 317, 266
Stockman A., 2019, Current Opinion in Behavioral Sciences, 30, 87
Stockman A., Sharpe L. T., 2000, Vision Research, 40, 1711
Toledo D., Irwin P. G. J., Teanby N. A., Simon A. A., Wong M. H., Orton G. S., 2018, Geophys. Res. Lett., 45, 5329
Wildt R., 1934a, Göttinger Nachrichten, 67, 5
Wildt R., 1934b, Nature, 134, 418
Young A. T., 1985, S&T, 69, 399

APPENDIX A: COLOURIMETRY

The response of the human eye to colour is reviewed by Stockman (2019). In summary, the colours are perceived by the cone receptors of the human retina, which are divided into cones sensitive to short, medium, and long wavelengths across the visible spectrum. The standard definitions of the response functions for these S, M, and L receptors is defined by the CIE (http://www.cvrl.org). The CIE define the spectral responses of an average human eye, regarding either a 2° or 10° field of view, with the 10° responsivities, $l_{10}(\lambda)$, $m_{10}(\lambda)$, and $s_{10}(\lambda)$, now held to be 'standard', and shown in Fig. 5. When regarding a coloured object the visible spectrum stimulates the three cone types differently, giving a 'tri-stimulus' response that the typical human eye then perceives as colour. Since the cone sensitivities have broad wavelength responses, it is quite possible for humans to perceive two distinctly different flux spectra $F(\lambda)$ as having the same colour.

The colour of a real object is simulated on a computer monitor as a combination of three different distinct RGB colours (red, green, blue), or in print media via the CMYK system (cyan, magenta, yellow, black). For computer monitors the RGB pixels are usually narrow-wavelength bands centred on 645, 526, and 444 nm, but there is considerable variability between different devices. To try to standardize the treatment of colour in computer devices, Microsoft and HP defined the standard RGB system (sRGB) in 1996, which is now the standard colour space used by most computer devices and also the World Wide Web. To represent the colour of an object in sRGB we need to determine the correct combination of RGB that gives the same tri-stimulus response as the actual object would to the human eye. This is done, for monochromatic wavelengths, by filling one half of an incident field of view with light of a test wavelength and then filling the other half with a combination of R, G, and B and adjusting the relative brightnesses until both halves appear the same to an 'average' human observer. For many wavelengths, this is possible with positive brightnesses of R, G, and B, but for some wavelengths it is necessary to add one RGB colour to the test wavelength and then balance with the other two. In other words we need a negative contribution from one of the RGB colours. Wavelengths for which this happens are said to be 'out of gamut' and cannot quite be simulated with sRGB. The resulting functions that relate the LMS to RGB responses for monochromatic test colours are called the Colour Matching Functions (CMFs).

Because of the non-standard nature of RGB systems and also the fact that it is not quite possible to reproduce all LMS responses with positive contributions of three individual narrow colours, the CIE have defined the XYZ colour space, for which the CMFs (available at http://www.cvrl.org) are positive at all wavelengths. With these CMFs it is then possible to calculate the XYZ tri-stimulus responses

as, for example

$$X = \int_0^\infty F(\lambda)x(\lambda)d\lambda, \tag{A1}$$

where $F(\lambda)$ is the incident flux, $x(\lambda)$ is the colour-matching function for the X-component, and similarly for the Y- and Z-components. The responses are then normalized such that $X + Y + Z = 1$, and thus only two components need to be specified to complete describe the colour of the object.

Once the tri-stimulus response XYZ has been determined in the XYZ colour space, it can be converted to different colour space via a linear transform. As noted before, the sRGB colour space is not quite as standard as we might hope, but in this work we have assumed:

$$\begin{pmatrix} R \\ G \\ B \end{pmatrix} = \begin{pmatrix} 2.4934969 & -0.9313836 & -0.4027108 \\ -0.8294890 & 1.7626641 & 0.0236247] \\ 0.0358458 & -0.0761724 & 0.9568845 \end{pmatrix} \begin{pmatrix} X \\ Y \\ Z \end{pmatrix},$$

where the transformation matrix from XYZ to sRGB is that of http://www.russellcottrell.com/photo/matrixCalculator.htm.

In addition to modelling the average human eye's perception of colour, we also need to model the average human eye's perception of different intensities. Unlike the charged-coupled device (CCD) arrays in a camera, the eye does not respond linearly to incident intensity. Instead the response is more logarithmic, which is a good evolutionary strategy as it allows a larger dynamic range and thus good sensitivity to what might be lurking in the dark next to bright objects in the field of view. However, a result of this non-linear response is that when a camera records an image and converts the RBG responses into, typically, 8 bits per colour per pixel, a simple linear digitization leads to poor results in the digitized image. This is because not enough bits are allocated to measuring the variation of brightness over darker parts of the image, while too many are allocated to recording the variation in brighter parts of the image that the human eye cannot differentiate very well. Hence, prior to digitization, the linear R, G, and B responses are first normalized to the maximum of $[R, G, B]$ in the image (and thus all be in the range [0, 1]), and then these linear responses, $C_{\rm linear}$ (where $C_{\rm linear}$ represents $R_{\rm linear}$, $G_{\rm linear}$, $B_{\rm linear}$), are converted via the Gamma correction (https://www.w3.org/Graphics/Color/sRGB.html) to

$$C_{sRGB} = \begin{cases} 12.92C_{linear}, & C_{linear} \leq 0.0031308 \\ 1.055C_{linear}^{1/\gamma} - 0.055, & C_{linear} > 0.0031308 \end{cases},$$

where in this sRGB definition $\gamma = 2.4$. The pixel values are then digitized. This leads to an efficient digitization of the image. However, for a computer to then display the image with the correct intensity ratios, the inverse correction needs to be applied by the monitor

$$C_{linear} = \begin{cases} \frac{C_{sRGB}}{12.92}, & C_{sRGB} \leq 0.04045 \\ \left(\frac{C_{sRGB}+0.055}{1.055}\right)^{\gamma}, & C_{sRGB} > 0.04045 \end{cases},$$

where the $C_{\rm sRGB}$ pixel values (i.e. $R_{\rm sRGB}$, $G_{\rm sRGB}$, $B_{\rm sRGB}$) have first been normalized to the maximum of the gamma-corrected [$R_{\rm sRGB}$, $G_{\rm sRGB}$, $B_{\rm sRGB}$] pixel values in the image, and thus be in the range [0, 1], and again, $\gamma = 2.4$.

This inverse gamma-correction is automatically applied by computer monitors and printers as it is assumed that all images to be displayed have already been gamma-corrected. The value of γ is 2.4 by definition in sRGB, but alternative values are sometimes used by different monitors.

For further reading on how colour is perceived by the human eye and properly rendered, the reader may also find this website from Andrew T. Young useful: https://aty.sdsu.edu/explain/optics/color/color.html.

APPENDIX B: CONVERSION BETWEEN MAGNITUDE AND DISC-AVERAGED REFLECTIVITY

The Lowell Observatory disc-integrated magnitudes of Uranus and Neptune reported by Lockwood (2019) and Lockwood & Jerzykiewicz (2006) are calculated as

$$m = -2.5\log\left(\frac{F_P}{F_V}\right), \tag{B1}$$

where F_P and F_V are the observed fluxes (W m^{-2}) of the planet and the standard reference star, Vega, respectively, integrated over the specified wavelength filter, that is,

$$F_V = \int_0^\infty V(\lambda)f(\lambda)d\lambda, \tag{B2}$$

where $V(\lambda)$ is the flux spectrum (W m^{-2} μm^{-1}) of Vega and $f(\lambda)$ is the filter transmission spectrum, while for the planet

$$F_P = \int_{\lambda=0}^{\lambda=\infty}\int_{\omega=0}^{\omega=\Omega_P} R_P(\lambda, r, \phi)\frac{S(\lambda)}{\pi}f(\lambda)d\omega d\lambda, \tag{B3}$$

where $S(\lambda)$ is the solar flux spectrum (W m^{-2} μm^{-1}) at the planet, $R_P(\lambda, r, \phi)$ is the reflectivity of a point on the planet at wavelength λ, radial distance from centre of planet's disc r, and azimuth angle ϕ, and $d\omega$ is the solid angle of the element. The total solid angle of the planetary disc is Ω_P.

Averaging over the disc, equation (B3) can be simplified to

$$F_P = \frac{\Omega_P}{\pi}\int_0^\infty \overline{R_P(\lambda)}S(\lambda)f(\lambda)d\lambda, \tag{B4}$$

where $\overline{R_P(\lambda)}$ is the disc-averaged reflectivity at each wavelength. To a good approximation, equation (B4) can be approximated for the Lowell Observatory Ice Giant magnitude data by

$$F_P \sim \overline{R}_P\frac{\Omega_P}{\pi}\int_0^\infty S(\lambda)f(\lambda)d\lambda, \tag{B5}$$

where $\overline{R}_P$ is the filter- and disc-averaged reflectivity of the planet. Substituting for F_P and F_V into equation (B1), we find

$$m \sim -2.5\log\left(\frac{\overline{R}_P\frac{\Omega_P}{\pi}\int_0^\infty S(\lambda)f(\lambda)d\lambda}{\int_0^\infty V(\lambda)f(\lambda)d\lambda}\right), \tag{B6}$$

which can be rearranged to recover disc-averaged reflectances from the magnitude data

$$\overline{R}_P \sim \frac{\pi}{\Omega_P}\frac{\int_0^\infty V(\lambda)f(\lambda)d\lambda}{\int_0^\infty S(\lambda)f(\lambda)d\lambda}10^{-\frac{m}{2.5}}. \tag{B7}$$

As noted in the manuscript, the magnitudes quoted by Lockwood & Jerzykiewicz (2006) and Lockwood (2019) for Uranus have been scaled to those that would be observed from the Earth with Uranus at a distance of 19.191 au from the Sun and 18.191 au from the Earth. The reference Vega (Colina, Bohlin & Castelli 1996)), Solar (Chance & Kurucz 2010), and Uranus (Irwin et al. 2022) spectra are compared

in Fig. 9, together with the location of Strömgren *b*, *y* filters, Johnson B, V filters, and the *HST*/WFC3 F467M and F547M filters. The ratio of the filter-averaged fluxes in equation (B7)

$$\frac{\int_0^\infty V(\lambda) f(\lambda) d\lambda}{\int_0^\infty S(\lambda) f(\lambda) d\lambda} \tag{B8}$$

is found to be 115.196 and 79.8838 for the Strömgren *b* and *y* filters, respectively, assuming the distance of Uranus from the Sun is 19.191 au.

This paper has been typeset from a TEX/LATEX file prepared by the author.